A Computational Model for Intergranular Stress Corrosion Cracking

Thesis by

Julián J. Rímoli

In Partial Fulfillment of the Requirements

for the Degree of

Doctor of Philosophy

California Institute of Technology

Pasadena, California

2009

(Defended May 5, 2009)

To my wife Analía

Acknowledgements

I would like to express my deep gratitude to Professor Michael Ortiz for giving me the opportunity to join his group. He has guided me through the process of becoming a scientist and supported all of my academic endeavors. His wealth of ideas, expertise, and variety of academic interests have had a profound impact on my own growth as a researcher. Similarly, I am indebted to my dear friend and former advisor Professor Marcos Actis from Universidad Nacional de La Plata for his constant mentorship, encouragement and support. His problem-solving approach to engineering has always guided me when addressing new scientific challenges, and his passion for teaching cultivated my own. Likewise, I will always be thankful to Professor Pablo Zavattieri and Dr. Eduardo Dvorkin for introducing me to the fascinating field of computational mechanics.

I would also like to acknowledge Professors Guruswami Ravichandran, Chiara Daraio and Swaminathan Krishnan for their guidance and participation in my examination committee. Their ideas and suggestions are certainly imprinted in the outcomes of this work. Likewise, I would like to recognize the help of Dr. Ercan Gurses regarding topics in his areas of expertise such as crystal plasticity and crack propagation modeling. I am glad that my interactions with Ercan went beyond academic matters, evolving into a strong friendship.

I am thankful for the friends I found at Caltech. Benny, J-T, Kakani, Andrew, Daniel and Tamer have supported me throughout the process of adapting to the life in a new

country. The moments we shared will never be forgotten. In addition, fellow group members Luigi, Celia, Lenny, Ben, Feras, Vikram, Santiago, Alejandro, Jarek and Yash made the office a fun place to work. A special recognition deserve my dearest friends Bo, Gabriela, Marcial and Matias for their constant support and for being always by my side in the ups and downs of a five-year long process.

I am glad I met Marta and Lydia, the central pillars of the group. Their careless support and love for the students made a real difference in our lives. Every single day was more enjoyable because of them.

I am grateful to my family in Argentina: my parents, my sisters Carla and Mari, and my sisters in-law Luchi and Car. Their genuine love, care and support is much appreciated.

Finally, I would like to express my deep gratitude to my wife Analia for her unconditional love, encouragement and support over the last seventeen years of my life. She has always been the central part of every decision I took, every choice I made and every path I followed. She has pushed me to find my intellectual limits and inspired my work by leading by example. She has always provided wisdom and emotional balance and I firmly believe she has always been the key for my success. For all of this, and much more that cannot be expressed in simple words, she deserves credit for every achievement I have accomplished as much as I do. As we always say Ana: “we are a team!”.

Abstract

Stress corrosion cracking (SCC) is a very common failure mechanism characterized by a slow, environmentally induced crack propagation in structural components. Time-to-failure tests and crack-growth-rate tests are widespread practices for studying the response of various materials undergoing SCC. However, due to the large amount of factors affecting the phenomenon and the scattered data, they do not provide enough information for quantifying the effects of main SCC mechanisms. This thesis is concerned with the development of a novel 3-dimensional, multiphysics model for understanding the intergranular SCC of polycrystalline materials under the effect of impurity-enhanced decohesion. This new model is based upon: (i) a robust algorithm capable of generating the geometry of polycrystals for objects of arbitrary shape; (ii) a continuum finite element model of the crystals including crystal plasticity; (iii) a grain boundary diffusion model informed with first-principles computations of diffusion coefficients; and (iv) an intergranular cohesive model described by concentration-dependent constitutive relations also derived from first-principles. Results are validated and compared against crack-growth-rate and initiation time tests.

Contents

List of Figures

List of Tables

List of Algorithms

Chapter 1

Introduction

1.1 Stress corrosion cracking fundamentals

Stress corrosion cracking (SCC) is a very common failure mechanism characterized by a slow, environmentally induced crack propagation in structural components [9]. As a consequence of SCC, cracks develop in otherwise non-cracking systems conveying a macroscopic loss of mechanical properties, which may affect the performance of structures and mechanical systems [10] or even cause a catastrophic failure [11].

For SCC to occur the simultaneous presence of tensile stress, corrosive environment and a susceptible material is required (figure 1.1). The stress corrosion cracking behavior of a given system largely depends on the applied stress, the geometry of the mechanical component or structural element, the presence of impurities or alloying elements in the material, as well as its strength and microstructure.

Stress corrosion cracking is a phenomenon that has an impact on several technological applications ranging multiple length scales. It may affect large structures such as bridges and nuclear reactors as well as sub-milimeter thick gun barrel coatings.

The mechanisms of SCC in metals can be classified as (i) anodic mechanisms, e.g., active dissolution and removal of material from the crack tip; and (ii) cathodic mechanisms, e.g.,

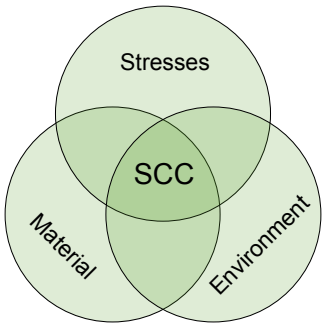

Figure 1.1: Stress corrosion cracking factors.

hydrogen evolution, adsorption, diffusion and embrittlement. The present work is focused on the latter group, particularly on the study of stress corrosion cracking by impurity-enhanced decohesion.

It is widely known that impurity segregation on grain boundaries of polycrystalline metals can induce intergranular embrittlement. This phenomenon is usually referred to as impurity-enhanced decohesion, and is of great importance in technological applications.

Several research efforts have attempted to explain and understand the underlying mechanisms of intergranular embrittlement. A representative example of this effort is the work by Yamaguchi et al. [12], where they try to address why and how sulfur weakens the grain boundaries of nickel by means of first principles computations. The authors found that a short-range overlap repulsion among densely segregated and neighboring sulfur atoms causes a large grain boundary expansion. They claim that this expansion facilitates the grain boundary decohesion process by reducing the grain boundary tensile strength by one order of magnitude. Their results are in good agreement with the experimental findings of Heuer et al. [13].

In a recent article, Yamaguchi [14] extended his work to study the decohesion of ferro-

magnetic BCC iron grain boundaries by sulfur or phosphorous segregation. As a result, he found two main embrittlement mechanisms where the predominance of one of them over the other depends on the impurity being segregated. The main mechanism for the sulfur-induced decohesion was found to be fracture surface stabilization with reference to the grain boundary by the segregated solute atoms without interaction between them. In the case of phosphorous-induced embrittlement, the predominant mechanism was claimed to be due to grain boundary destabilization by a repulsive interaction among the segregated and neighboring solute atoms. They conclude that this difference in the predominant decohesion mechanism makes sulfur a much stronger embrittling element than phosphorous.

Another interesting work is the one performed by Krupp et al. [15] on oxygen-induced intergranular fracture of the nickel-base alloy IN718 during mechanical loading at high temperatures. This nickel-based superalloy, commonly used in high-temperature high-strength components in gas turbines, exhibits a change in the failure mechanism when loaded slowly at temperatures above 600^{o} C. It has been observed that the cycle-dependent fatigue failure produces a time-dependent intergranular brittle fracture [16] [17] [18] [19] [20]. Even though several authors have attributed this transition to grain boundary oxidation, one of the principal findings of their experimental study is that oxygen-induced intergranular fracture does not necessarily requires the formation of oxides. Furthermore, their work suggest that oxygen-enhanced decohesion might be the predominant mechanism of intergranular fracture at high temperature.

Krupp's hypothesis is supported by first-principles calculations performed by Yamaguchi and Kaburaki [21]. They found that the formation energy of NiO per oxygen atom is larger than or comparable to the grain boundary segregation energy of oxygen. In addition, their findings show that oxygen has a strong embrittlement effect when segregated to the grain

boundary.

Despite the nature of the predominant decohesion mechanism for a given system, it is clear that the presence of impurities may have a strong embrittlement effect on the grain boundary cohesive energy and this is precisely the effect we intend to capture through our model.

1.2 Motivation

Even though gun barrel erosion is unlikely to cause catastrophic failure of artillery systems, its effect on eroded bores largely affects the gun system performance, including range and accuracy loss, directional stability loss (with its consequent dispersion), excessive torsional impulse and a reduction in the barrel fatigue life [10]. Consequently, the operational effectiveness of a gun system may be considerably affected by erosion, making evident the need to develop models able to understand and predict it.

Over the last decade, a number of efforts have been made to model and simulate several mechanisms present in gun barrel erosion. A salient example of these efforts is the recently work published by Sopok and coworkers [23] [24]. They developed a series of thermal-chemical-mechanical gun bore erosion models for advanced artillery systems. Although these models have achieved some degree of success, they require several experimental inputs for calibration purposes. As a consequence, a strictly predictive model capable of replacing experiments and aid gun system design does not exist yet.

As pointed out by Sopok and coworkers, gun barrel erosion is mainly dominated by the development of stress corrosion cracks. Both anodic and cathodic mechanisms are associated with gun barrel erosion. The former mechanism is mainly observed on the substrate at points where the coating may present cracks. The latter mechanism is observed at the

coating-substrate interface as well as on deeper levels within the substrate. Figure 1.2 shows a schematic representation of gun barrel erosion and its main mechanisms.

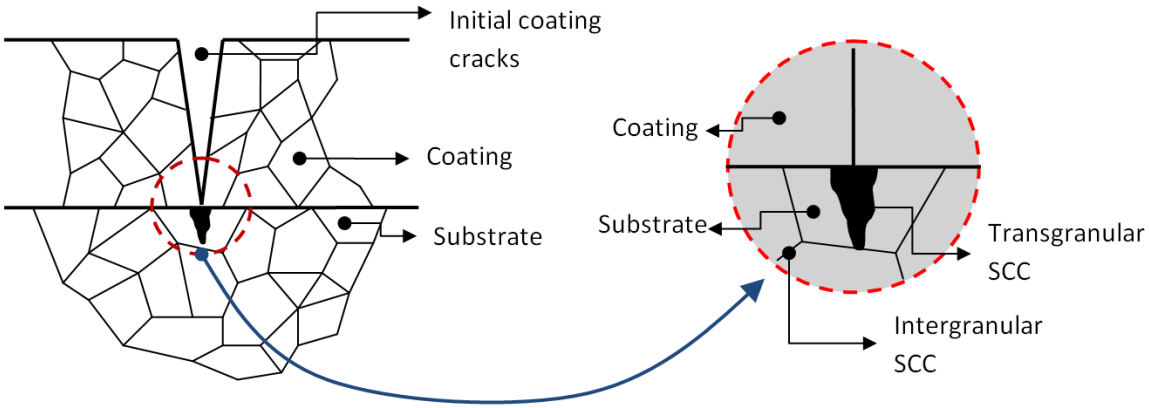

Figure 1.2: Schematics of gun barrel erosion.

The problem of gun barrel erosion is therefore a complex phenomenon which encompasses different regions where different damage mechanisms are present. Thus, it is a logical approach to divide those mechanisms and study them separately.

In a recent work, Bjerken and coworkers [25] studied the stress-driven material dissolution where the loss of atoms to the environment may lead to crack growth (i.e., anodic SCC). They showed that the interaction of the dissolution process and the mechanical loads render local irregularities that develop into pits and notches and eventually into cracks. Furthermore, they found that these cracks resemble the type of pits encountered on gun barrel substrates right at the points where pre-cracks due to manufacturing processes are present on the coating (see figure 1.3).

The goal of this thesis it to contribute to a deeper understanding of the gun barrel erosion phenomenon by focusing on modeling the effects of impurity enhanced decohesion on the substrate (i.e., cathodic SCC). This constitutes a fundamental step to developing a model of wear for gun barrels accounting for the coupling between chemistry, mechanics

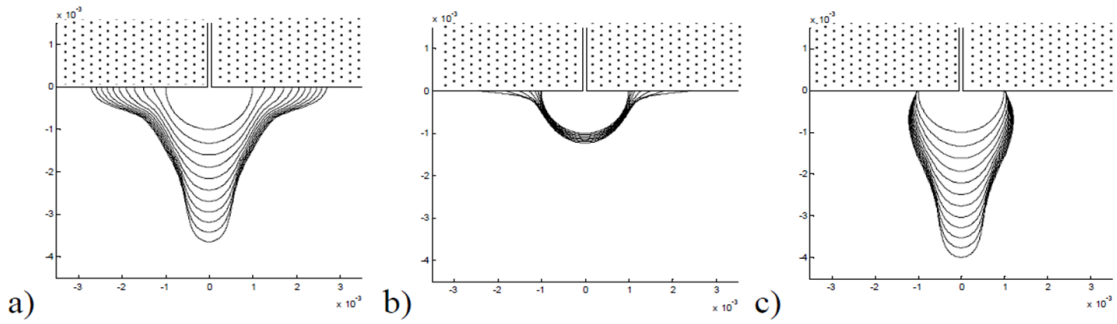

Figure 1.3: Simulated gun barrel pit.

and thermal analysis capable of predicting wear rates and mechanisms for advanced artillery systems.

1.3 Model fundamentals

The proposed model for intergranular stress corrosion cracking is based upon: (i) a robust algorithm capable of generating the geometry of polycrystals for objects of arbitrary shape; (ii) a continuum finite element model of the crystals including crystal plasticity; (iii) a grain boundary diffusion model informed with first-principles computations of diffusion coefficients; and (iv) an intergranular cohesive model described by concentration-dependent constitutive relations also derived from first-principles.

A brief description of each aspect of the model is presented in the following subsections.

1.3.1 Generation of polycrystalline geometries

A systematic methodology for generating 2 and 3-dimensional polycrystal geometries was developed as follows. At first, a given initial coarse mesh representing the object to be modeled is refined by means of the longest edge bisection algorithm originally proposed by Rivara and Levin [26]. Then, a barycentric subdivision of the resulting mesh is performed

from which a barycentric dual is defined [27]. The grains defined in this way may have very non convex shapes making necessary the implementation of a final step to correct this issue. To this end, the grain boundaries are relaxed by means of a minimization of the total grain boundary area.

The details of this methodology are discussed in chapter 2.

1.3.2 Grain boundary diffusion model

In order to account for the effect of impurity diffusion across the grain boundaries, Fisher's grain boundary diffusion model [28] was adopted and specialized for the case of Harrison's type C kinetic regime [29]. The only input required for this continuum model is the grain boundary diffusion coefficient which may be obtained from first principles computations or experimental data.

The implemented grain boundary diffusion model is developed in chapter 3.

1.3.3 Polycrystal model

Once the polycrystalline geometry is defined, one random lattice rotation $\mathbf{R}$ is assigned to each grain in the model. For a single grain, its elastic response is modeled by a cubic elastic behavior whereas the plastic response is captured by means of a crystal plasticity model, which accounts for the different slip systems present in the material as well as the different critical resolved shear stress for each system.

The polycrystal model is described in depth in chapter 4.

1.3.4 Intergranular cohesive fracture model

The intergranular cohesive fracture model is one of the principal components of the present approach. Cohesive elements, as originally developed by Ortiz and Pandolfi [30], are placed at every grain boundary. In order to account for the embrittlement due to the presence of impurities, a cohesive response depending on the concentration of impurities [22] is adopted. This impurity-dependent cohesive response is informed by first-principles calculations.

The details of the intergranular cohesive fracture model are discussed in chapter 4.

1.3.5 Solution procedure

All the aspects of the model where integrated through a single C++ program. The multi-physics aspects of the model were addressed by means of a staggered procedure described in detail in chapter 5.

Chapter 2

Generation of polycrystalline geometries

2.1 Introduction

The intergranular stress corrosion cracking model proposed in the present thesis accounts for the effect of the microstructure on the mechanical response of the material by explicitly considering the geometry of each grain. This approach is usually referred to as direct numerical simulation (DNS) of polycrystals.

Generating an adequate geometric representation of the grain size distribution and three-dimensional grain shapes is usually an intricate aspect of the DNS approach. To this end, several strategies have been proposed ranging from phase field models of grain growth [31] to level sets methods for modeling the evolution of faceted crystals [32]. Nevertheless, these approaches constitute a research area by themselves and their use is not straightforward to implement in current finite element programs.

A simpler approach consists of assuming isotropic and uniform grain growth during solidification. The resulting grains can be identified as the Voronoi cells corresponding to a given initial distribution of 0-cells or nucleation points. As a drawback of this approach, it is difficult to generate a Voronoi diagram for arbitrary geometries. Consequently, the shape

of the element being modeled is highly restricted. In addition, the resulting grains can be difficult to triangulate by means of a tetragonal mesh.

To address the pitfalls of the previous approach, it is common to adopt a structured mesh to represent the grain geometries. In this approach, each grain is represented by a tetrakaidecahedron [33] [34]. This method allows us to easily generate finite element meshes. Unfortunately, this approach is also restrictive regarding the shape of the element being modeled making it very difficult, if not impossible, to model objects other than cuboids.

This chapter deals with the development of a new method for generating geometric representations of objects made of polycrystalline materials. The proposed method can naturally be applied to model objects of any shape given their initial triangulation. Furthermore, a finite element mesh is produced as a standard outcome of the method.

In the following sections a brief overview of the method is presented followed by a more detailed explanation of each aspect of it. We conclude the chapter with some examples showing the capabilities of the method.

2.2 Overview of the method

The method developed in this thesis for generating geometric representations of polycrystalline objects can be conceptually divided into two stages. The first one consists of a series of purely geometric algorithms, which lead to a first definition of the domain for each grain. This representation usually results in very non-convex grains. Thus, a second stage is required in which the grain boundaries are relaxed so that the resulting grains have a more convex shape.

The first stage, which we refer to as geometric stage, requires the input of an initial mesh which might be just a coarse representation of the geometry of the object under

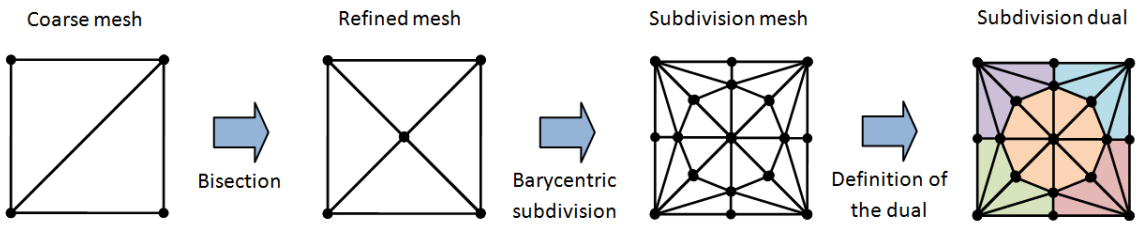

Figure 2.1: Schematic representation of the geometric stage of polycrystal generation.

consideration. Given the initial mesh, the following tasks are performed:

1. Refinement of the initial mesh.

2. Barycentric subdivision of the refined mesh.

3. Definition of the domain for each grain (barycentric dual).

A schematic representation of the geometric stage is depicted in figure 2.1. The figure shows the procedure for the two-dimensional case for illustration purposes.

As mentioned before, the procedure depicted above may lead to very non-convex grain geometries. To deal with this issue, the second stage of our method consists on the application of a grain boundary relaxation algorithm. Figure 2.2 shows the evolution of two typical grains as a result of this relaxation.

2.3 Geometric step

For the first task of the geometric stage, i.e., the mesh refinement, a well established longest edge bisection algorithm [26] was implemented. More generally, the refined mesh can be generated by any commercial mesh generation package. Consequently, in this section the focus is placed on the generation of the barycentric subdivision mesh and the definition of the corresponding subdivision dual. Some background information on simplicial complexes is presented in the next subsection to facilitate the understanding of the developed algorithms.

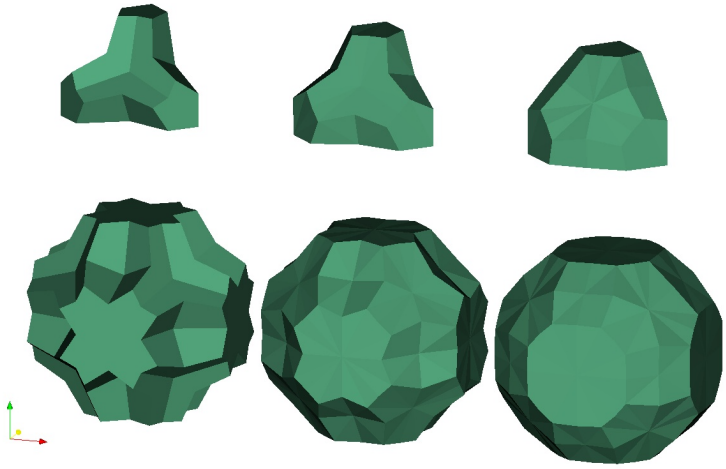

Figure 2.2: Evolution of two typical grains with constant grain boundary energy.

2.3.1 Brief background on simplicial complexes

A cell complex is a collection of objects, or cells, to which a precise dimension can be assigned. At its fundamental level, a 3-dimensional object can be represented by a collection of 0-cells (vertices), 1-cells (edges), 2-cells (faces) and 3-cells (volumes). In the subsequent paragraphs, p-dimensional cells are denoted as e_p. In addition, $E_p(\mathcal{S})$ represents the collection of p-dimensional cells in a complex $\mathcal{S}$. The dimension $\dim \mathcal{S}$ of the cell complex $\mathcal{S}$ is the largest dimension of any of its cells. Special classes of cell complexes are obtained when the cells are restricted to be of a certain type.

Particularly, if the cells are required to be simplices we obtain simplicial complexes. This type of complexes arises in practice when bodies are discretely represented by means of triangulations. In order to introduce the concept of simplicial complexes a definition of simplices must be first introduced.

Let $v_0, ..., v_p$ be a geometrically independent set in $\mathbb{R}^n$. The simplex σ spanned by

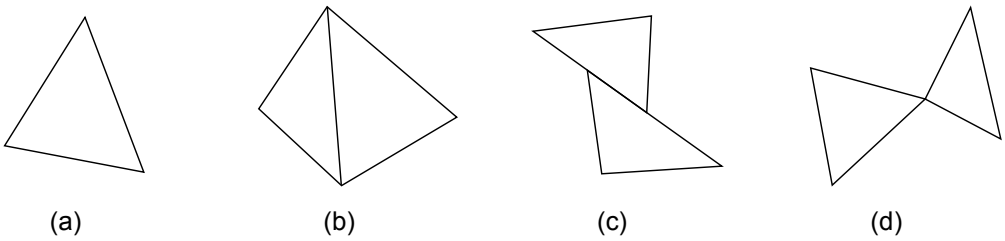

Figure 2.3: Examples of collection of simplices (after [1]).

$v_0, ..., v_p$ is defined as

$$\sigma = \left\{ x \in \mathbb{R}^n : \quad \sum_{i=0}^{p} \lambda_i = 1, \quad \sum_{i=0}^{p} \lambda_i v_i = x, \quad \lambda_i \geq 0 \quad \forall i = 0, 1, ..., p \right\} \tag{2.1}$$

where the numbers λ_i are called the barycentric coordinates of x with respect to $v_0, ..., v_p$. The barycentric coordinates of a point are uniquely determined by it. The points $v_0, ..., v_p$ can be geometrically interpreted as the vertices of the simplex σ and p as its dimension. Any simplex generated by a subset of $v_0, ..., v_p$ is a proper face of σ and the union of all proper faces is defined as the boundary of the simplex. The notation $e_\beta \prec e_\alpha$ signifies that e_β is a face of e_α.

A simplicial complex $\mathcal{S}$ in $\mathbb{R}^n$ is a collection of simplices in $\mathbb{R}^n$ such that

1. Every face of a simplex of $\mathcal{S}$ is in $\mathcal{S}$.

2. The intersection of any two simplices of $\mathcal{S}$ is a face of each of them.

Figure 2.3 shows several examples of collections of simplices. It is clear from the definition of a simplicial complex that (a), (b) and (d) are simplicial complexes whereas (c) is not a simplicial complex.

2.3.2 Barycentric subdivision

Generally speaking, a subdivision complex is obtained by subdividing the cells of a given cell complex into finer cells. Let $\mathcal{S}$ be a cell complex. A complex $\mathcal{B}$ is said to be a subdivision of $\mathcal{S}$ if:

1. Every cell of Y is contained in a cell of X.

2. Every cell of X is the union of finitely many cells of Y.

These conditions particularly imply that the union of the cells of $\mathcal{B}$ equals the union of the cells of $\mathcal{S}$ and, hence, $|\mathcal{B}| = |\mathcal{S}|$ as sets. The way in which a subdivision complex $\mathcal{B}$ is nested within the supercomplex $\mathcal{S}$ may be described by means of an inclusion map $f : \mathcal{B} \to \mathcal{S}$. This map assigns to every cell e_β of $\mathcal{B}$ the cell e_α of $\mathcal{S}$ that contains it. The so called barycentric subdivision generates a particular class of subdivision complexes.

The barycentric subdivision of a simplicial complex is obtained by means of a uniform refinement. If $\sigma_p = [v_0, ..., v_p]$ is a p-simplex of a simplicial complex $\mathcal{S}$, its barycenter is the point

$$\hat{\sigma}_p = \sum_{i=0}^{p} \frac{1}{p+1} v_i \tag{2.2}$$

i.e., the barycenter is the point in the interior of σ_p that has equal barycentric coordinates.

Given a simplicial complex $\mathcal{S}$ its barycentric subdivision $\mathcal{B}$ consists of all simplices $[\hat{\sigma}_0, ..., \hat{\sigma}_p]$ such that $\hat{\sigma}_0 \succ ... \succ \hat{\sigma}_p$. As an example, figure 2.4 shows the barycentric subdivision of a triangle.

The algorithm implemented to perform the barycentric subdivision of an arbitrary simplicial complex is detailed in algorithm 1.

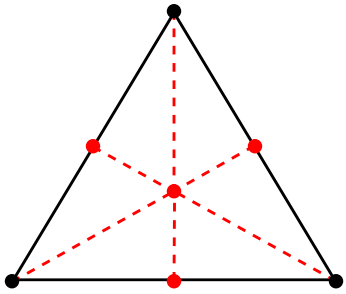

Figure 2.4: Barycentric subdivision of a triangle.

Algorithm 1: Barycentric subdivision.

Input: simplicial complex $\mathcal{S}$, $n = \dim \mathcal{S}$.
Output: barycentric complex $\mathcal{B}$.
`/* Initialize barycentric complex` $\mathcal{B}$ `and inclusion map` f `*/`
for $(p = 0, ..., n)$ **do**
  for $(e_p \in E_p(\mathcal{S}))$ **do**
    insert v in $E_0(\mathcal{B})$;
    insert (e_p, v) in f;
`/* Compute connectivity table` $CT(\mathcal{S})$ `*/`
for $(e_n \in E_n(\mathcal{S}))$ **do**
  insert $[e_n]$ in $CT(\mathcal{S})$;
for $(p = n, ..., 1)$ **do**
  for $([e_n, ..., e_p] \in CT(\mathcal{S}))$ **do**
    for $(e_{p-1} \prec e_p)$ **do**
      append e_{p-1} to $[e_n, ..., e_p]$;
`/* Compute connectivity table` $CT(\mathcal{B})$ `*/`
for $([e_n, ..., e_0] \in CT(\mathcal{S}))$ **do**
  insert $[f(e_n), ..., f(e_0)]$ in $CT(\mathcal{B})$;
construct the simplicial complex $\mathcal{B}$ from $CT(\mathcal{B})$;
return $\mathcal{B}$

2.3.3 Dual definition

The barycentric subdivision alone does not define the region corresponding to each grain in the model. To achieve this goal, the concept of dual mesh has to be introduced. An in-depth discussion of the concepts of duality can be found in [1] and [27]. For a more intuitive approach see [2] and [35]. For computational aspects and implementation of duality concepts on computer codes see [36].

The main idea underlying the notion of dual mesh is to associate to each primal k-simplex of the n-dimensional cell complex $\mathcal{S}$ a dual $(n-k)$-cell of the dual complex $\mathcal{B}$. For example, for each 0-cell in a 2-dimensional cell complex a dual 2-cell can be defined. Each 1-cell will have associated a 1-cell in the dual mesh and each primal 2-cell can be associated to a dual 0-cell. Figure 2.5 shows a 2-dimensional example of primal and dual cells.

To determine the domain corresponding to each grain in the polycrystal, we adopt the concept of dual cells. Grains are then defined as dual cells on the barycentric complex $\mathcal{B}$ corresponding to primal 0-cells on the refined mesh represented by the simplicial complex $\mathcal{S}$.

Let e_0 be a 0-cell in the n-dimensional cell complex $\mathcal{S}$ and $\hat{e}_0 = f(e_0)$ the corresponding 0-cell on $\mathcal{B}$ given by the inclusion map f. The n-dimensional grain associated to e_0 is given by the set of n-cells belonging to $\mathcal{B}$ incident to $\hat{e}_0$, i.e., $I_n = \{e_n \succ f(e_0)\}$. To complete the construction of the simplicial complex (mesh) associated to a given grain, the set of $(0, ..., n-1)$-cells incident to each element of I_n must be inserted into the complex without repetition.

The corresponding computational implementation of grain domain definition is presented in detail in algorithm 2.

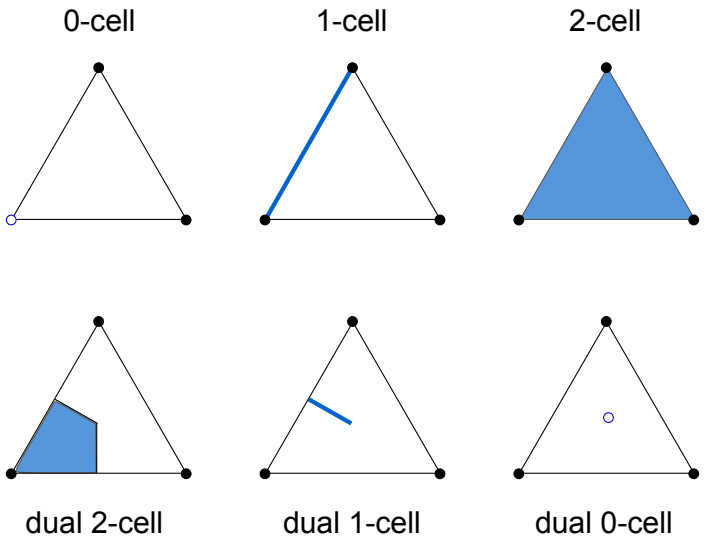

Figure 2.5: 2-dimensional example of primal and dual cells (after [2]).

Algorithm 2: Grain domain definition.

Input: simplicial complex $\mathcal{S}$, $n = \dim \mathcal{S}$, barycentric complex $\mathcal{B}$, inclusion map f.
Output: map form cell to grain subcomplex $\mathcal{PC}$.

initialize map form cell to grain subcomplex $\mathcal{PC}$;
for $e_0 \in E_0(\mathcal{S})$ **do**
    initialize subcomplex $\mathcal{G}$ with dimension n;
    insert $I_n = \{e_n \succ f(e_0)\}$ in $E_n(\mathcal{G})$;
    for $(p = n, ..., 1)$ **do**
        for $(e_p \in E_p(\mathcal{G}))$ **do**
            insert, without repetition, $I_{p-1} = \{e_{p-1} \prec e_p\}$ in $E_{p-1}(\mathcal{G})$;
    insert $(e_0, \mathcal{G})$ in $\mathcal{PC}$;
return $\mathcal{PC}$

2.4 Grain boundary relaxation step

The grains generated with the algorithms described in the previous section are usually very non-convex in opposition to experimental observations. Thus, a convexification algorithm had to be implemented. Basically, it consists of two steps:

1. Extraction of grain boundaries from the original polycrystal mesh.

2. Minimization of the total grain boundary area with respect to the nodal positions.

Once the grain boundary area is expressed in terms of nodal coordinates, the process of numerically attaining its minimum is not trivial. Two algorithms were implemented, namely a gradient flow algorithm (algorithm 3) and a non-linear version of the conjugate gradient algorithm (algorithm 4).

When the conjugate gradient algorithm was employed, convergence was eventually achieved but at a rate too slow to be of practical use for problems involving more than 1,000 grains. On the other hand, when the minimization was pursued by means of the non-linear conjugate gradient algorithm, the problem diverged in the first few steps.

In our experience, the best approach was to start the minimization with a gradient flow algorithm so that the solution gets closer to the minimum. After a few steps, the algorithm is interrupted and the conjugate gradient solver takes over the process. In this way, a minimum is usually attained after less than 50 iterations even for problems involving more than thousands of grains.

Figure 2.6 shows the evolution of a polycrystal mesh undergoing grain boundary area minimization. It is clearly observed that the resulting grains are much more convex than those on the starting mesh.

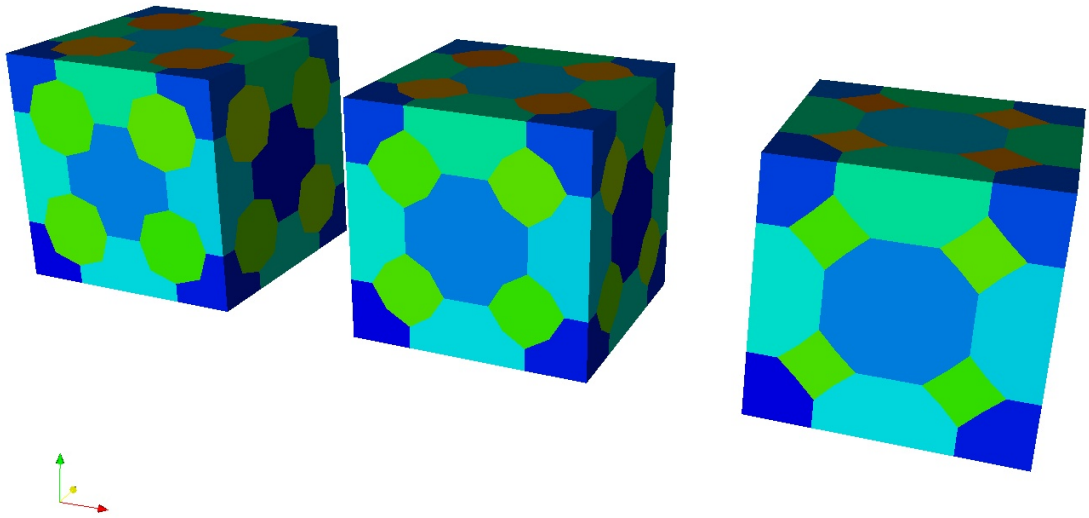

Figure 2.6: Relaxation of a polycrystal with constant grain boundary energy.

Algorithm 3: Gradient flow.

Input: field x, force function $DE(\cdot)$, maximum iterations N, tolerance T, small number ε.

```
for (k = 0, ..., N) do
    u ← −DE(x) · ε;
    x ← x + u;
    Error ← ‖u‖;
    if (Error < T) then
        update local state;
        return SUCCESS;
return FAIL;
```

Algorithm 4: Non-linear conjugate gradient.

Input: field x, force function $DE(\cdot)$, maximum iterations N, tolerance T, small number ε.

$\alpha \leftarrow \beta \leftarrow dr \leftarrow 0$;
$r \leftarrow DE(x)$;
$r_n \leftarrow r$;
$d \leftarrow r$;
for $(k = 0, ..., N)$ **do**
  $x \leftarrow x + \varepsilon \cdot d$;
  $dr \leftarrow \frac{(DE(x)-r)\cdot d}{\varepsilon}$;
  $\alpha \leftarrow \alpha - \frac{r\cdot d}{dr} - \varepsilon$;
  $x \leftarrow x + \alpha \cdot d$;
  $r_n \leftarrow DE(x)$;
  $Error \leftarrow \|r_n\|$;
  if $(Error < T)$ **then**
    update local state;
    return `SUCCESS`;
  $\beta \leftarrow \frac{r_n(r_n-r)}{r^2}$;
  if $(\beta < 0)$ **then**
    $\beta = 0$;
  $d \leftarrow r_n + \beta \cdot d$;
  $r \leftarrow r_n$;
return `FAIL`;

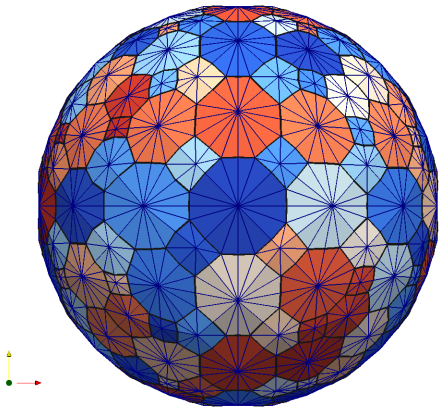

Figure 2.7: Polycrystalline sphere.

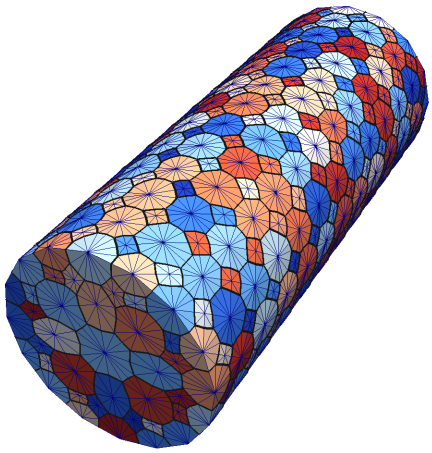

Figure 2.8: Polycrystalline rod.

2.5 Examples

In this section, a few examples demonstrating the capabilities of the method developed in the present chapter are presented. Figures 2.7 and 2.8 show the ability of the method to generate polycrystalline structures for complex geometries. Figure 2.9 shows how the method can produce meshes with grains of different sizes. Finally, figure 2.10 shows an example where the mesh produced by the method was refined after the grain geometry was generated.

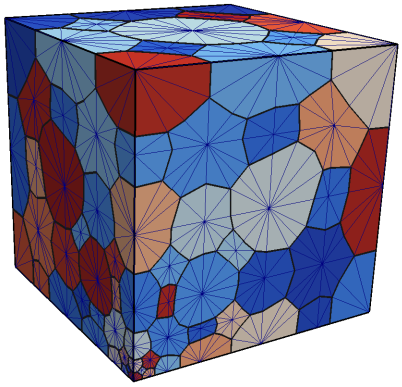

Figure 2.9: Polycrystal with grain size variation according to a power law.

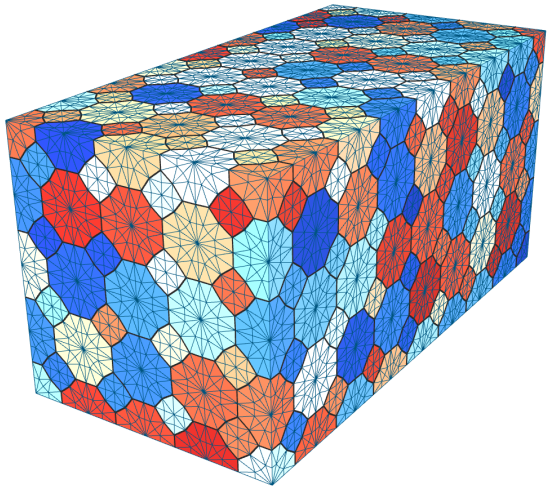

Figure 2.10: Polycrystalline cuboid. Its grain were refined after the geometry generation algorithm was completed.

Chapter 3

Grain boundary diffusion model

3.1 Introduction

Grain boundaries are the interfaces between two grains in a polycrystalline material. They are highly disordered almost two dimensional regions (only a few atoms in thickness) that provide, in general, less resistance to atomic movements than the adjacent grains. Within this context, grain boundary diffusion may be defined [37] as the process of atomic transport due to random motion of atoms along the grain boundaries in crystalline materials.

Understanding grain boundary diffusion is fundamental for comprehending the more complex phenomenon of stress corrosion cracking by impurity-enhanced decohesion. Grain boundary diffusion is the driving mechanism that facilitates the transport of impurities from the corrosive environment to the core of the material.

The present chapter will start by stating Fick's [38] laws of diffusion; later, Fisher's [28] widely accepted theory of grain boundary diffusion will be presented, followed by the standard classification of grain boundary diffusion regimes originally introduced by Harrison [29]. A relationship between first principles computations and phenomenological diffusion coefficients will be established. To conclude, the methods and algorithms necessary to address the grain boundary diffusion phenomenon will be presented: finite elements discretization

and discrete time integration.

3.2 Fick's laws of diffusion

In 1855 German physiologist Adolf Eugen Fick [38] recognized the analogy between diffusion and heat transfer by conduction and established Fick's laws of diffusion. The first law states that the diffusant flux $\mathbf{q}$ is proportional to the diffusant concentration gradient. In mathematical terms this can be expressed as

$$\mathbf{q} = -\mathbf{D}\nabla c \tag{3.1}$$

where c is the diffusant concentration, $\mathbf{D}$ is the diffusion coefficient and ∇ is the gradient operator defined (using Einstein's notation) as

$$\nabla = \mathbf{e}^i \frac{\partial}{\partial x^i}$$

Fick's second law relates the diffusant flux $\mathbf{q}$ at a given point to its concentration rate of change by means of the equation

$$\frac{\partial c}{\partial t} = -\nabla \mathbf{q} \tag{3.2}$$

Under the assumption of independence of $\mathbf{D}$ on position, we can substitute 3.1 into 3.2 obtaining

$$\frac{\partial c}{\partial t} = \mathbf{D}\nabla^2 c \tag{3.3}$$

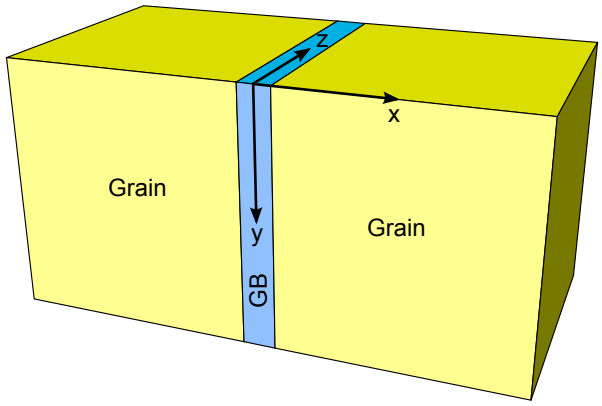

Figure 3.1: Grain boundary schematics: grains shown in yellow, grain boundary of thickness δ in light blue.

where ∇^2 is the Laplacian operator of the form

$$\nabla = \frac{\partial^2}{\partial x^i x^i}$$

Equation 3.3 is usually called the diffusion equation.

3.3 Fisher's grain boundary diffusion model

Let us consider an isolated grain boundary as schematically shown in figure 3.1. Grains (with diffusion coefficient D_g) are shown in yellow whereas the grain boundary zone (with diffusion coefficient D_{gb}) of thickness δ is shown in light blue.

In 1950 Fisher [28] developed the first model of grain boundary diffusion for this kind of system. Even though there were other attempts to model this phenomenon (e.g., [39], [40] and [41]), recent literature reviews (e.g., [42], [43]) indicate that Fisher's model is still the only one used for the analysis of the experimentally determined penetration profiles of the

isotope diffusing along the grain boundaries.

Fisher's model is based on four fundamental assumptions that can be summarized as follows:

1. Fick's laws of diffusion are obeyed both at the grains and at the grain boundary.

2. Both the diffusant concentration and the flux are continuous across the grain/grain boundary interface.

3. The grain boundary is so thin that concentration variation along its width (i.e., along the x-axis direction) is negligible.

4. The diffusion coefficients D_g and D_{gb} are isotropic and independent of concentration, position and time.

In mathematical terms, assumption (1) can be expressed by means of two diffusion equations:

$$\frac{\partial c_g}{\partial t} = D_g \left(\frac{\partial^2 c_g}{\partial x^2} + \frac{\partial^2 c_g}{\partial y^2} + \frac{\partial^2 c_g}{\partial z^2} \right) \qquad if\ |x| > \frac{\delta}{2} \tag{3.4a}$$

$$\frac{\partial c_{gb}}{\partial t} = D_{gb} \left(\frac{\partial^2 c_{gb}}{\partial x^2} + \frac{\partial^2 c_{gb}}{\partial y^2} + \frac{\partial^2 c_{gb}}{\partial z^2} \right) \qquad if\ |x| \leq \frac{\delta}{2} \tag{3.4b}$$

In addition, assumption (2) allows us to couple equations 3.4a and 3.4b. Mathematically, this can be expressed as the boundary conditions

$$c_g(x, y, z, t) = c_{gb}(x, y, z, t) \qquad if |x| = \frac{\delta}{2} \tag{3.4c}$$

$$\mathbf{q}_g(x, y, z, t) = \mathbf{q}_{gb}(x, y, z, t) \qquad if |x| = \frac{\delta}{2} \tag{3.4d}$$

To simplify the former expressions, c_{gb} can be expanded in Taylor-series around $x = 0$

obtaining

$$c_{gb} = c_{gb}\Big|_{x=0} + x\frac{\partial c_{gb}}{\partial x}\Big|_{x=0} + \frac{x^2}{2}\frac{\partial^2 c_{gb}}{\partial x^2}\Big|_{x=0} + ...$$

Under assumption (3), higher order terms can be neglected, and assuming symmetry of c_{gb} with respect to the yz plane its expansion becomes

$$c_{gb} = c_{gb}\Big|_{x=0} + \frac{x^2}{2}\frac{\partial^2 c_{gb}}{\partial x^2}\Big|_{x=0} \tag{3.5}$$

Replacing the previous approximation for c_{gb} in equation 3.4b, evaluating it at $x = \pm\frac{\delta}{2}$, and neglecting terms of order δ^2 the following expression is obtained:

$$\frac{\partial}{\partial t}\left(c_{gb}\Big|_{x=0}\right) = D_{gb}\frac{\partial^2 c_{gb}}{\partial x^2}\Big|_{x=0} + D_{gb}\left(\frac{\partial^2}{\partial y^2}\left(c_{gb}\Big|_{x=0}\right) + \frac{\partial^2}{\partial z^2}\left(c_{gb}\Big|_{x=0}\right)\right) \tag{3.6}$$

Finally, plugging 3.5 into 3.4d results in the equation

$$D_{gb}\frac{\partial^2 c_{gb}}{\partial x^2}\Big|_{x=0} = \frac{2D_g}{\delta}\frac{\partial c_g}{\partial x} \tag{3.7}$$

By replacing the previous equation in 3.6 and considering 3.8a, Fisher's representation of the grain boundary diffusion problem is obtained:

$$\frac{\partial c_g}{\partial t} = D_g\left(\frac{\partial^2 c_g}{\partial x^2} + \frac{\partial^2 c_g}{\partial y^2} + \frac{\partial^2 c_g}{\partial z^2}\right) \qquad if\ |x| > \frac{\delta}{2} \tag{3.8a}$$

$$\frac{\partial c_{gb}}{\partial t} = D_{gb}\left(\frac{\partial^2 c_{gb}}{\partial y^2} + \frac{\partial^2 c_{gb}}{\partial z^2}\right) + \frac{2D_g}{\delta}\frac{\partial c_g}{\partial x} \qquad if\ |x| \leq \frac{\delta}{2} \tag{3.8b}$$

Both equations are still coupled by the condition

$$c_g(x, y, z, t) = c_{gb}(x, y, z, t) \qquad if|x| = \frac{\delta}{2} \tag{3.8c}$$

Equations 3.8a and 3.8b are known as Fisher's equations of grain boundary diffusion. It can be observed that 3.8b became a two dimensional diffusion equation in the grain boundary area. The first term in the right hand side represents the diffusion within the grain boundary whereas the second term accounts for the leakage of diffusant to the adjacent grains.

3.4 Grain boundary diffusion regimes

Typically, the grain boundary diffusion phenomenon involves more than plain transport of atoms along the grain boundaries; it is a complex combination of several elementary processes among which the most important ones are:

1. Pure diffusion along the grain boundaries.

2. Leakage of impurity atoms from the grain boundaries to the bulk.

3. Diffusion through the bulk.

The relative importance of each elementary process usually varies for different material/impurity systems, and within the same system for different grain sizes and temperatures. This variation determines the global behavior of the system under consideration, resulting in different kinetic regimes.

The first analysis of grain boundary diffusion kinetics was performed by Harrison [29] in 1961. In his work, Harrison introduced three kinetic regimes which he called types A, B and C (figure 3.2).

Even though other classifications were proposed in the subsequent years (e.g., [37], [41] for general grain boundary diffusion or [44] for mobile grain boundaries), Harrison's

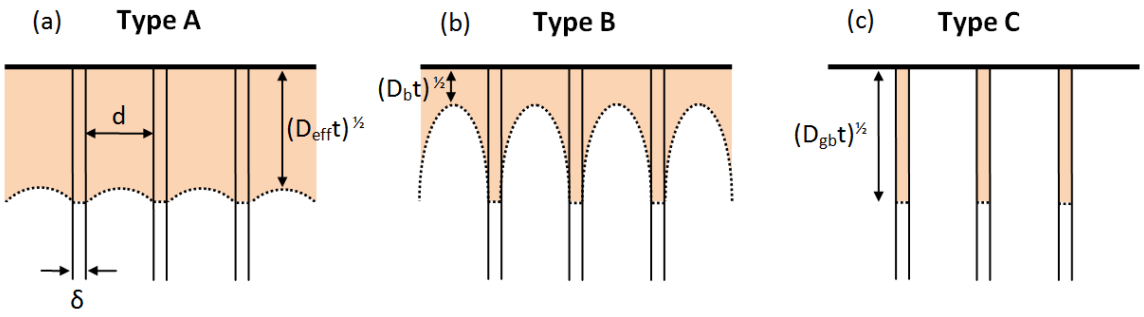

Figure 3.2: Schematic representation of types A, B and C diffusion kinetics following Harrison's classification.

categorization of diffusion kinetics for polycrystals still is the most widely adopted by the scientific community.

3.4.1 Type A kinetics

The A regime is observed in the limiting case of high temperatures and/or very long anneal time and/or small grain sizes, and/or bulk diffusion coefficient not much smaller than the grain boundary diffusion coefficient.

In this regime, the diffusant is not only confined to the grain boundary: during the diffusion anneal, a migrating atom may pass from a grain boundary to the crystal lattice and it may then diffuse through the grain until it reaches another grain boundary.

If the anneal time is long enough, the atom may visit several grains as well as several grain boundaries. Thus, the macroscopic behavior under regime A conditions appears to obey Fick's law for a homogeneous medium with some effective diffusion coefficient D_{eff} (figure 3.2a). Following Hart [45], the effective diffusion coefficient in the A regime can be estimated as

$$D_{eff} = gD_g + (1-g)D_{gb} \tag{3.9}$$

where g is the volume fraction of the grains in the polycrystal.

3.4.2 Type B kinetics

The B regime is observed at lower temperatures, and/or shorter anneal time and/or larger grain sizes than those that favor the occurrence of regime A kinetics.

Even though the diffusant is not only confined to the grain boundary as in regime A, the typical bulk diffusion constant is smaller in this case when compared to the grain boundary diffusion constant than in the previous regime. As a result, the diffusant is not homogeneously distributed across the polycrystal: high concentrations are encountered at the grain boundaries, rapidly decreasing into the grains (figure 3.2b).

Under type B kinetic conditions, the polycrystal cannot be thought of as a homogeneous medium anymore, and a full solution of Fisher's model (equations 3.8a and 3.8b) is needed to fully capture the phenomenon.

3.4.3 Type C kinetics

The C regime generally is observed in the other limiting case of low temperatures and/or short anneal time and/or large grain sizes, and/or bulk diffusion coefficient much smaller than the grain boundary diffusion coefficient.

In this regime, the bulk diffusion is almost locked and diffusion takes place almost exclusively at the grain boundaries without any essential leakage to the neighboring grains (figure 3.2c).

When type C kinetics is present, the transport of the diffusant is governed by only one diffusion coefficient: the grain boundary diffusion coefficient D_{gb}. Thus, Fisher's system can be reduced to one single differential equation:

$$\frac{\partial c_{gb}}{\partial t} = D_{gb}\left(\frac{\partial^2 c_{gb}}{\partial y^2} + \frac{\partial^2 c_{gb}}{\partial z^2}\right) \qquad if\ |x| \leq \frac{\delta}{2} \tag{3.10}$$

3.5 Determination of the grain boundary diffusion coefficient

Let us consider the first principle computations commonly performed to estimate the values of diffusion coefficients. Such simulations usually place impurity atoms into a matrix and measure the mean square distance they travel as a function of time. At a constant temperature T, the mean square distance $\langle d^2 \rangle_T$ scales linearly with time. Thus, it is possible to perform a linear fit of the first-principles computations results. That is,

$$\langle d^2 \rangle_T = m_T t \tag{3.11}$$

where m_T is the slope of the linear fit and t the time. It is also known that the mean square distance relates to the diffusion coefficient D_T at temperature T as follows

$$\langle d^2 \rangle_T = 2 D_T t \tag{3.12}$$

Consequently, it is possible to eliminate the time from the equations and obtain a relation between the slope and the diffusion coefficient obtaining

$$m_T = 2 D_T \tag{3.13}$$

By assuming that the dependence of the diffusion coefficient on time is given by an Arrhenius equation, the following relations can be expressed for two different temperatures T_1 and T_2

$$m_{T_1} = 2 D_0 e^{-\frac{E_a}{R T_1}} \tag{3.14}$$

$$m_{T_2} = 2 D_0 e^{-\frac{E_a}{R T_2}} \tag{3.15}$$

where D_0 is the pre-exponential factor, E_a the activation energy and R the gas constant. It is possible, then, to identify the unknowns by performing first-principles computations of the mean square distance at two given temperatures. Thus, by solving the previous equations a final expression for the diffusion coefficient can be expressed as

$$D(T) = D_0 e^{-\frac{E_a}{RT}} \tag{3.16}$$

with D_0 and E_a given by

$$D_0 = \frac{m_{T_2}}{2}\left(\frac{m_{T_2}}{m_{T_1}}\right)^{\frac{T_1}{T_2-T_1}} \tag{3.17}$$

$$E_a = R\frac{T_1 T_2}{T_2 - T_1}\ln\left(\frac{m_{T_2}}{m_{T_1}}\right) \tag{3.18}$$

Utilizing data provided by Van Duin [8] (see table 3.1), making an average of the values for different types of grain boundaries and following the procedure depicted above the following estimation for the grain boundary diffusion coefficient for H in Fe (in m^2/s) is obtained:

$$Dfp_{gb}(T) = 2.44 \cdot 10^{-7} \exp\left(-\frac{1334.42}{T}\right) \tag{3.19}$$

Table 3.1: First principles values of D_{gb} in $[A^2/ps]$ for H in Fe [8]

Type of GB	D_{gb} **at 500K**	D_{gb} **at 1500K**
Σ3[110][111]	2.82	16.18
Σ5[001][210]	1.13	6.73
Σ5[001][310]	1.61	9.57
Σ7[111][321]	2.01	12.40
Σ13[001][320]	1.53	9.08
Σ13[001][510]	1.34	7.98
Σ17[001][530]	1.39	8.25
Average	1.69	10.03

Analogously, following the same procedure for experimental values reported in the lit-

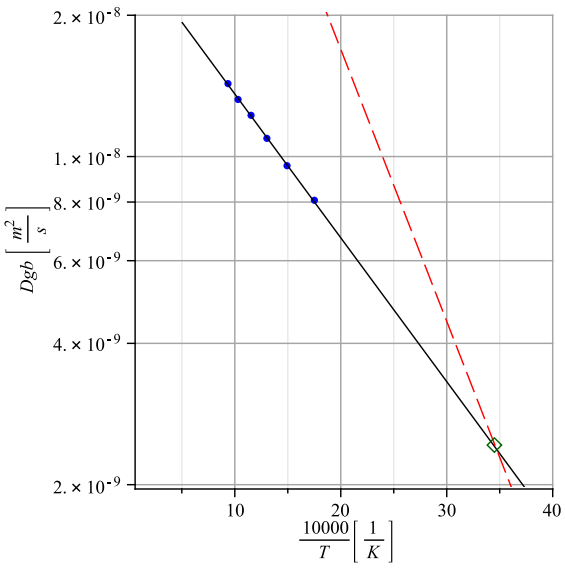

Figure 3.3: Estimation of grain boundary diffusion coefficient for H in Fe. Experimental values [3] (solid circles), experimental fit (solid line), first principles fit (dashed line) and estimated value at room temperature (empty diamond).

erature [3], the following fit is obtained

$$Dexp_{gb}(T) = 2.75 \cdot 10^{-8} \exp\left(-\frac{705.46}{T}\right) \tag{3.20}$$

As shown in figure 3.3, the fits for first principles computations and experiments show a considerable disagreement. The values obtained form first principles computations are considerably higher than those reported experimentally. This could be due to the fact that all of the grain boundary simulated were pure tilt grain boundaries. This kind of boundary provides an array of parallel dislocations which could facilitate pipe diffusion along the grain boundaries. Nevertheless, their value is almost identical at room temperature, the one selected for our validations.

3.6 Finite element implementation

3.6.1 Spatial discretization

3.6.1.1 Strong form

In general, the diffusion problem in $\mathbb{R}^n$ can be described in a local, strong form by means of a differential equation and appropriate boundary conditions.

As seen before, the diffusion equation on a domain Ω can be expressed as

$$\frac{\partial c}{\partial t} + \frac{\partial q^i}{\partial x^i} = 0 \qquad in\ \Omega \tag{3.21}$$

where c is the impurity concentration and q^i represent the components of the flux vector expressed in an orthonormal basis with coordinates x^i. The corresponding boundary conditions are given by

$$c = \bar{c} \quad on\ \partial\Omega_1 \qquad q^i = \bar{q}^i \quad on\ \partial\Omega_2 \tag{3.22}$$

where $\partial\Omega_1$ and $\partial\Omega_2$ must satisfy

$$\partial\Omega_1 \cup \partial\Omega_2 = \partial\Omega, \quad \partial\Omega_1 \cap \partial\Omega_2 = \emptyset \tag{3.23}$$

3.6.1.2 Weak form

The same problem can also be described in an integral or weak form. In order to accomplish that, let us consider the weighting functions w satisfying

$$w \quad such\ that \quad \int_\Omega \frac{\partial w}{\partial x^i} d\Omega < \infty \quad and \quad w = 0 \quad on\ \partial\Omega_1 \tag{3.24}$$

Multiplying the diffusion equation by the weighting function and integrating over the domain, it becomes

$$\int_\Omega \left(w \frac{\partial c}{\partial t} + w \frac{\partial q^i}{\partial x^i} \right) d\Omega = 0 \tag{3.25}$$

Noting that

$$w \frac{\partial q^i}{\partial x^i} = \frac{\partial}{\partial x^i} \left(w \, q^i \right) - \frac{\partial w}{\partial x^i} q^i \tag{3.26}$$

it can be expressed as

$$\int_\Omega \left(w \frac{\partial c}{\partial t} + \frac{\partial}{\partial x^i} \left(w \, q^i \right) - \frac{\partial w}{\partial x^i} q^i \right) d\Omega = 0 \tag{3.27}$$

The previous expression can be now easily integrated by parts obtaining

$$\int_\Omega \left(w \frac{\partial c}{\partial t} - \frac{\partial w}{\partial x^i} q^i \right) d\Omega + \int_{\partial\Omega} w \, q^i \, n_i \, dS = 0 \tag{3.28}$$

In addition, $w = 0$ on $\partial\Omega_1$ and $q^i = \bar{q}^i$ on $\partial\Omega_2$. Therefore, the weak form of the diffusion problem in $\mathbb{R}^n$ can be expressed as

$$\int_\Omega \left(w \frac{\partial c}{\partial t} - \frac{\partial w}{\partial x^i} q^i \right) d\Omega + \int_{\partial\Omega_2} w \, \bar{q}^i \, n_i \, dS = 0 \tag{3.29}$$

3.6.1.3 Constitutive relation

In order to establish a link between the concentration c and the flow $\mathbf{q}$, a constitutive relation must be assumed. As stated in previous sections of this chapter, the constitutive relation is assumed to be of Fick's type. It can be derived from the energy density

$$W(\boldsymbol{\psi}) = \frac{1}{2} D^{jk} \psi_j \psi_k \tag{3.30}$$

where $\psi_i = \frac{\partial c}{\partial x^i}$ and D^{jk} is the diffusion coefficient. Within this context, the flux $\mathbf{q}$ is given by

$$q^i = -\frac{\partial W(\boldsymbol{\psi})}{\partial \psi_i} \tag{3.31}$$

The energy derivative can be computed as follows:

$$\frac{\partial W(\boldsymbol{\psi})}{\partial \psi_i} = \frac{1}{2} D^{jk} \frac{\partial \psi_j}{\partial \psi_i} \psi_k + \frac{1}{2} D^{jk} \psi_j \frac{\partial \psi_k}{\partial \psi_i} \tag{3.32}$$

Considering that $\frac{\partial \psi_j}{\partial \psi_i} = \delta_{ji}$, $\frac{\partial \psi_k}{\partial \psi_i} = \delta_{ki}$ it becomes

$$\frac{\partial W(\boldsymbol{\psi})}{\partial \psi_i} = \frac{1}{2} D^{ik} \psi_k + \frac{1}{2} D^{ji} \psi_j \tag{3.33}$$

The symmetry of the diffusion coefficient tensor $\mathbf{D}$ implies that

$$\frac{\partial W(\boldsymbol{\psi})}{\partial \psi_i} = D^{ij} \psi_j \tag{3.34}$$

As a result, the flux $\mathbf{q}$ can be expressed as

$$q^i = -D^{ij} \psi_j = -D^{ij} \frac{\partial c}{\partial x^j} \tag{3.35}$$

Finally, by plugging it into the weak form it becomes

$$\int_\Omega \left(w \frac{\partial c}{\partial t} + \frac{\partial w}{\partial x^i} D^{ij} \frac{\partial c}{\partial x^j} \right) d\Omega + \int_{\partial \Omega_2} w \, \bar{q}^i \, n_i \, dS = 0 \tag{3.36}$$

3.6.1.4 Discretization

The discretization of equation 3.36 will now be performed. In order to do that, c and w are interpolated using the shape functions N_i and the nodal values $\hat{c}_i$ and $\hat{w}_i$. That is,

$$w = N_a \hat{w}_a \quad ; \quad c = N_b \hat{c}_b \quad ; \quad \vec{q}^{\,i} = N_b \hat{\vec{q}}^{\,i}_b \tag{3.37}$$

Thus, the respective derivatives can be expressed as

$$\frac{\partial w}{\partial x^i} = \frac{\partial N_a}{\partial x^i}\hat{w}_a \quad ; \quad \frac{\partial c}{\partial x^j} = \frac{\partial N_b}{\partial x^j}\hat{c}_b \quad ; \quad \frac{\partial c}{\partial t} = N_b \frac{\partial \hat{c}_b}{\partial t} \tag{3.38}$$

Therefore, plugging the previous interpolations into 3.36 the following expression is obtained:

$$\int_\Omega \left(N_a \hat{w}_a N_b \frac{\partial \hat{c}_b}{\partial t} + \frac{\partial N_a}{\partial x^i}\hat{w}_a D^{ij} \frac{\partial N_b}{\partial x^j}\hat{c}_b \right) d\Omega + \int_{\partial\Omega_2} N_a \hat{w}_a \, N_b \hat{\vec{q}}^{\,i}_b \, n_i \, dS = 0 \tag{3.39}$$

Since the equation above must hold for all weighting functions w, the following identity must hold

$$\left(\int_\Omega N_a N_b d\Omega \right) \frac{\partial \hat{c}_b}{\partial t} + \left(\int_\Omega \frac{\partial N_a}{\partial x^i} D^{ij} \frac{\partial N_b}{\partial x^j} d\Omega \right) \hat{c}_b = - \int_{\partial\Omega_2} N_a N_b \hat{\vec{q}}^{\,i}_b \, n_i \, dS \tag{3.40}$$

In order to simplify the notation in previous equation, let us define

$$M_{ab} = \int_\Omega N_a N_b d\Omega \quad K_{ab} = \int_\Omega \frac{\partial N_a}{\partial x^i} D^{ij} \frac{\partial N_b}{\partial x^j} d\Omega \tag{3.41}$$

where M_{ab} and K_{ab} are called the mass and and stiffness matrices respectively by analogy

with solid mechanics problems. Let us also define the forcing term

$$Q_a = -\int_{\partial\Omega_2} N_a N_b \hat{\bar{q}}_b^i \, n_i \, dS \tag{3.42}$$

Therefore, equation 3.40 becomes

$$M_{ab}\frac{\partial \hat{c}_b}{\partial t} + K_{ab}\hat{c}_b = Q_a \tag{3.43}$$

Equation 3.43 is the discrete finite elements representation of the diffusion problem. As it can be seen, it represents a system of ordinary differential equations. The standard way of solving it is by numerical integration. In the next subsection, the general family of trapezoidal integrators adopted in this study is described.

3.6.2 Temporal discretization: generalized trapezoidal methods

The finite element discretization of the diffusion problem 3.43 can be expressed in matrix notation as

$$\mathbf{M}\cdot\dot{\mathbf{c}} + \mathbf{K}\cdot\mathbf{c} = \mathbf{Q} \tag{3.44}$$

As it can be seen, equation (3.44) represents a discretization of the diffusion problem in space. Therefore, a time-discretization is needed to solve the dynamic problem. The family of generalized trapezoidal methods assume the following time-discretization:

$$\mathbf{M}\cdot\dot{\mathbf{c}}_{n+1} + \mathbf{K}\cdot\mathbf{c}_{n+1} = \mathbf{Q}_{n+1} \tag{3.45a}$$

$$\mathbf{c}_{n+1} = \mathbf{c}_n + \Delta t\dot{\mathbf{c}}_{n+\alpha} \tag{3.45b}$$

$$\dot{\mathbf{c}}_{n+\alpha} = (1-\alpha)\mathbf{c}_n + \alpha\dot{\mathbf{c}}_{n+1} \tag{3.45c}$$

where α is a parameter between 0 and 1. Plugging (3.45c) into (3.45b) and defining $\mathbf{c}_{n+1}^{pred} = \mathbf{c}_n + \Delta t(1-\alpha)\dot{\mathbf{c}}_n$ the following expressions are obtained

$$\mathbf{c}_{n+1} = \mathbf{c}_{n+1}^{pred} + \alpha\Delta t\dot{\mathbf{c}}_{n+1} \tag{3.46a}$$

$$\dot{\mathbf{c}}_{n+1} = \frac{\mathbf{c}_{n+1} - \mathbf{c}_{n+1}^{pred}}{\alpha\Delta t} \tag{3.46b}$$

Finally, plugging (3.46b) into (3.45a) the following expression is obtained

$$\mathbf{M} \cdot \frac{\mathbf{c}_{n+1} - \mathbf{c}_{n+1}^{pred}}{\alpha\Delta t} + \mathbf{K} \cdot \mathbf{c}_{n+1} = \mathbf{Q}_{n+1} \tag{3.47}$$

Equation (3.47) can be solved for $\mathbf{c}_{n+1}$ and the obtained value plugged in (3.46b) to obtain $\dot{\mathbf{c}}_{n+1}$.

Chapter 4

Mechanical model

4.1 Introduction

This chapter deals with the development of the mechanical models necessary to represent the intergranular stress corrosion cracking phenomenon of polycrystalline materials undergoing impurity-enhanced decohesion.

It begins by briefly introducing the balance equations that govern both the mechanical behavior of the grains in the polycrystal as well as the cohesive response between them.

In section 4.3 the basic principles of thermodynamics which rule the existence of the equation of state, the conservation of energy and the direction in which processes take place are discussed. The obtained results in that section will be of crucial importance in the development of the constitutive models for crystal plasticity and cohesive surfaces performed in the subsequent sections.

In section 4.4 the mechanical response of the polycrystal is modeled, placing particular emphasis on the presentation of the constitutive model for the elastic-plastic response of single crystals.

To conclude the chapter, an intergranular cohesive fracture model that accounts for impurity effects on the grain boundaries is presented.

4.2 Balance equations

The present section introduces the balance equations that govern both the mechanical behavior of the grains in the polycrystal as well as the cohesive response between them. After a brief description of the kinematic considerations and the corresponding notation, the equations of conservation of mass, linear momentum and angular momentum are developed. For a complete discussion of the topics addressed here see references [46] and [47].

4.2.1 Kinematic considerations

Let us consider the deformation of a body occupying a domain $\mathcal{B} \in \mathbb{R}^3$ in a certain reference configuration. The material points $P \in \mathcal{B}$ are labeled by means of their coordinates $\mathbf{X}(P)$ on some reference frame, which we call the material reference frame.

Furthermore, let us consider a one-to-one deformation mapping $\boldsymbol{\varphi} : \mathcal{B} \rightarrow \mathbb{R}^3$. This mapping completely defines the motion of the body, ruling out interpenetration of matter and tearing. In this way, the coordinates $\mathbf{x}$ of a given material point at a given time are expressed as

$$\mathbf{x}(t) = \boldsymbol{\varphi}(\mathbf{X}, t), \quad \mathbf{X} \in \mathcal{B} \tag{4.1}$$

Consequently, the current configuration Ω at a given time t is defined as the mapping of the entire reference configuration, that is,

$$\Omega(t) = \boldsymbol{\varphi}(\mathcal{B}, t) \tag{4.2}$$

The material velocity field is given by the material time derivative of the deformation

map

$$\mathbf{v}(t) = \left.\frac{\partial \boldsymbol{\varphi}}{\partial t}\right|_{\mathbf{X}} \tag{4.3}$$

Analogously, the material acceleration field is given by the second time derivative of the deformation map

$$\mathbf{a}(t) = \left.\frac{\partial^2 \boldsymbol{\varphi}}{\partial t^2}\right|_{\mathbf{X}} \tag{4.4}$$

The action of the deformation mapping on an infinitesimal material vector $d\mathbf{X}$ at $\mathbf{X}$ is completely determined by the deformation gradient $\mathbf{F}$ which, when expressed in components, takes the form

$$F^i_J = \frac{\partial \varphi^i}{\partial X^J} \tag{4.5}$$

The deformed and undeformed oriented areas $d\mathbf{a}$ and $d\mathbf{A}$ are related by the Piola transformation

$$n_i \, da = J \, F^{I^{-1}}_i N_I \, dA \tag{4.6}$$

where $J = \det(\mathbf{F})$ is the Jacobian of the deformation, n_i the components of the unit normal to the area in the deformed configuration and N_I the components of the corresponding vector in the reference configuration.

Finally, the deformed and undeformed volumes are related by J as follows

$$dv = JdV \tag{4.7}$$

That is, the Jacobian is a direct measure of the volumetric deformation.

4.2.2 Conservation of mass

Let $\rho_0 : \mathcal{B} \to \mathbb{R}$ be the mass per unit undeformed volume and $\rho : \boldsymbol{\varphi}(\mathcal{B}) \to \mathbb{R}$ the current mass per unit deformed volume. The mass contained in an arbitrary sub-body $\mathcal{S} \in \mathcal{B}$ can be expressed as

$$m(\mathcal{S}) = \int_{\mathcal{S}} \rho_0(\mathbf{X})\, dV = \int_{\boldsymbol{\varphi}(\mathcal{S})} \rho(\mathbf{x})\, dv \tag{4.8}$$

Using equation 4.7 to transform the integral over the deformed configuration it becomes

$$\int_{\mathcal{S}} \rho_0(\mathbf{X})\, dV = \int_{\mathcal{S}} J\, \rho(\boldsymbol{\varphi}(\mathbf{X}))\, dV \tag{4.9}$$

Since $\mathcal{S}$ is arbitrary, for the previous equation to hold it is necessary that

$$\rho_0(\mathbf{X}) = J\, \rho(\boldsymbol{\varphi}(\mathbf{X})) \quad \text{in } \Omega = \boldsymbol{\varphi}(\mathbf{X}) \tag{4.10}$$

4.2.3 Conservation of linear momentum

As in the previous section, let us consider an arbitrary sub-body $\mathcal{S} \in \mathcal{B}$. The conservation of linear momentum can be expressed in the deformed configuration as

$$\int_{\partial\boldsymbol{\varphi}(\mathcal{S})} \mathbf{t}\, da + \int_{\boldsymbol{\varphi}(\mathcal{S})} \rho\, \mathbf{b}\, dv = \frac{d}{dt} \int_{\boldsymbol{\varphi}(\mathcal{S})} \rho\, \mathbf{v}\, dv \tag{4.11}$$

where $\mathbf{t}$ represents the traction, $\mathbf{b}$ the volumetric forces per unit mass and $\mathbf{v}$ the material velocity as defined by equation 4.3.

The traction $\mathbf{t}$ on a plane defined by the normal $\mathbf{n}$ is related to the Cauchy's stress

tensor $\boldsymbol{\sigma}$ as indicated by Cauchy's tetrahedron theorem:

$$\mathbf{t} = \boldsymbol{\sigma} \cdot \mathbf{n} \tag{4.12}$$

Inserting equation 4.12 into the equation of conservation of linear momentum, considering Reynolds' transport theorem (with mass conservation) to bring the time derivative into the integral and applying the divergence theorem, equation 4.11 becomes

$$\int_{\boldsymbol{\varphi}(\mathcal{S})} \operatorname{div}(\boldsymbol{\sigma})\, dv + \int_{\boldsymbol{\varphi}(\mathcal{S})} \rho\, \mathbf{b}\, dv = \int_{\boldsymbol{\varphi}(\mathcal{S})} \rho\, \mathbf{a}\, dv \tag{4.13}$$

In the previous expression $\mathbf{a}$ represents the material acceleration as defined in equation 4.4. Collecting terms it becomes

$$\int_{\boldsymbol{\varphi}(\mathcal{S})} \left[\operatorname{div}(\boldsymbol{\sigma}) + \rho\, \mathbf{b} - \rho\, \mathbf{a}\right]\, dv = \mathbf{0} \tag{4.14}$$

Since the previous identity must hold for any sub-body $\mathcal{S} \in \mathcal{B}$ it is a necessary condition that

$$\operatorname{div}(\boldsymbol{\sigma}) + \rho\mathbf{b} = \rho\mathbf{a} \quad \text{in } \Omega = \boldsymbol{\varphi}(\mathbf{X}) \tag{4.15}$$

Equation 4.15 is usually referred to as the local or strong form of the conservation of linear momentum.

4.2.4 Conservation of angular momentum

The integral statement of the conservation of angular momentum for a sub-body $\mathcal{S} \in \mathcal{B}$ can be expressed in spatial form as

$$\int_{\partial\boldsymbol{\varphi}(\mathcal{S})} \mathbf{x} \times \mathbf{t}\, da + \int_{\boldsymbol{\varphi}(\mathcal{S})} \mathbf{x} \times \rho\, \mathbf{b}\, dv = \frac{d}{dt} \int_{\boldsymbol{\varphi}(\mathcal{S})} \mathbf{x} \times \rho \mathbf{v}\, dv \tag{4.16}$$

As in the previous section, the application of Cauchy's tetrahedron theorem, Reynolds transport theorem (with mass conservation) and the divergence theorem results in

$$\int_{\boldsymbol{\varphi}(\mathcal{S})} \left\{ [\rho a_i - \rho b_i - \sigma_{ij,j}] + e_{ijk}\sigma_{jk} \right\} dv = 0 \tag{4.17}$$

Finally, assuming conservation of linear momentum we can see that the terms between brackets vanish. Thus,

$$\int_{\boldsymbol{\varphi}(\mathcal{S})} e_{ijk}\sigma_{jk}\, dv = 0 \tag{4.18}$$

Since the previous identity must hold for any sub-body $\mathcal{S} \in \mathcal{B}$ it is necessary that

$$e_{ijk}\sigma_{jk} = 0 \quad \text{in } \Omega = \boldsymbol{\varphi}(\mathbf{X}) \tag{4.19}$$

Due to the anti-symmetry of the permutation symbol it is necessary for $\boldsymbol{\sigma}$ to be symmetric in order to make the previous equation hold. Mathematically, it is expressed as

$$\boldsymbol{\sigma} = \boldsymbol{\sigma}^T \tag{4.20}$$

That is, the conservation of angular momentum implies the symmetry of Cauchy's stress tensor.

4.3 Thermodynamic aspects

A complete analysis of any problem in continuum mechanics cannot be performed without taking into account the principles of thermodynamics, which rule the existence of the equation of state, the conservation of energy and the direction in which processes take place. Therefore, the results obtained in this section will be of crucial importance in the development of the constitutive models for crystal plasticity and cohesive surfaces performed in subsequent sections of this chapter. For a more detailed discussion of the topics presented in this section as well as their application to constitutive theories see references [47], [46], [48] and [49].

4.3.1 Energy dissipation

Let us consider a sub-body $\mathcal{S} \in \mathcal{B}$. The external power of the forces acting on $\mathcal{S}$ is given by

$$P_{ext} = \int_{\partial\boldsymbol{\varphi}(\mathcal{S})} \mathbf{t} \cdot \mathbf{v}\, da + \int_{\boldsymbol{\varphi}(\mathcal{S})} \rho\, \mathbf{b} \cdot \mathbf{v}\, dv \tag{4.21}$$

Applying Cauchy's tetrahedron theorem and considering the symmetry of $\boldsymbol{\sigma}$ the previous expression becomes:

$$P_{ext} = \int_{\partial\boldsymbol{\varphi}(\mathcal{S})} (\boldsymbol{\sigma} \cdot \mathbf{v}) \cdot \mathbf{n}\, da + \int_{\boldsymbol{\varphi}(\mathcal{S})} \rho\, \mathbf{b} \cdot \mathbf{v}\, dv \tag{4.22}$$

This equation can be further transformed by means of the divergence theorem so that

$$P_{ext} = \int_{\boldsymbol{\varphi}(\mathcal{S})} \operatorname{div}(\boldsymbol{\sigma} \cdot \mathbf{v})\, dv + \int_{\boldsymbol{\varphi}(\mathcal{S})} \rho\, \mathbf{b} \cdot \mathbf{v}\, dv \tag{4.23}$$

Grouping terms and assuming conservation of linear momentum together with the sym-

metry of Cauchy's stress tensor $\boldsymbol{\sigma}$ the following expression is obtained

$$P_{ext} = \int_{\boldsymbol{\varphi}(\mathcal{S})} \boldsymbol{\sigma} : \mathrm{sym}(\nabla \mathbf{v})\, dv + \int_{\boldsymbol{\varphi}(\mathcal{S})} \frac{d}{dt}\left(\frac{1}{2}\rho\, \mathbf{v}\cdot\mathbf{v}\right)\, dv \tag{4.24}$$

Moreover, the application of Reynolds' transport theorem under the assumption of mass conservation allows us to take the time derivative out of the second integral, obtaining in this way

$$P_{ext} = \int_{\boldsymbol{\varphi}(\mathcal{S})} \boldsymbol{\sigma} : \mathrm{sym}(\nabla \mathbf{v})\, dv + \frac{d}{dt}\int_{\boldsymbol{\varphi}(\mathcal{S})} \left(\frac{1}{2}\rho\, \mathbf{v}\cdot\mathbf{v}\right)\, dv \tag{4.25}$$

Finally, after introducing the definition of the kinetic energy $K(t)$ of the sub-body $\mathcal{S} \in \mathcal{B}$ as

$$K(t) = \int_{\boldsymbol{\varphi}(\mathcal{S})} \left(\frac{1}{2}\rho\, \mathbf{v}\cdot\mathbf{v}\right)\, dv \tag{4.26}$$

the so called theorem of expended power [47] [50] is obtained:

$$P_{ext} = \int_{\boldsymbol{\varphi}(\mathcal{S})} \boldsymbol{\sigma} : \mathrm{sym}(\nabla \mathbf{v})\, dv + \frac{d}{dt}K(t) \tag{4.27}$$

As it can be seen, equation 4.27 implies that the total external power applied to the sub-body $\mathcal{S} \in \mathcal{B}$ is expended in part in the stress power and the rest contributes to a change in the kinetic energy of the sub-body.

The only assumptions during this derivation were the conservation of mass, linear and angular momentum. That is, there is not a single thermodynamic assumption in the previous result. It is in the subsequent parts of this section when thermodynamics comes into play with a decisive role.

Let us now consider the first law of thermodynamics for our sub-body $\mathcal{S} \in \mathcal{B}$ which postulates the existence of a function of state that measures the energy stored in the material.

The external power P_{ext} must be equal to the rate of dissipated energy P_{dis} plus the rate of stored internal energy P_{int} plus the rate of kinetic energy P_{kin}. That is,

$$P_{ext} = P_{kin} + P_{int} + P_{dis} \tag{4.28}$$

Considering the theorem of expended power given by equation 4.27 the previous expression becomes

$$P_{dis} = \int_{\boldsymbol{\varphi}(\mathcal{S})} \boldsymbol{\sigma} : \mathrm{sym}(\nabla \mathbf{v})\, dv - \frac{d\xi}{dt} \tag{4.29}$$

where ξ represents the energy stored in the material. Furthermore, in the spirit of the continuum theory the rate of dissipated energy density per unit of reference volume $\mathcal{D}$ is introduced as

$$P_{dis} = \int_{\mathcal{S}} \mathcal{D}\, dV \tag{4.30}$$

Along the same lines, it is also assumed that the energy stored in the material can be expressed in terms of a stored energy density per unit of reference volume e. That is,

$$\xi = \int_{\mathcal{S}} e\, dV \tag{4.31}$$

By introducing the two previous definitions into equation 4.29 it becomes

$$\int_{\mathcal{S}} \mathcal{D}\, dV = \int_{\boldsymbol{\varphi}(\mathcal{S})} \boldsymbol{\sigma} : \mathrm{sym}(\nabla \mathbf{v})\, dv - \int_{\mathcal{S}} \dot{e}\, dV \tag{4.32}$$

Expressing the first integral on the right hand side in terms of the reference configuration

and collecting terms, the following expression is obtained

$$\int_{\mathcal{S}} [\mathcal{D} - J\boldsymbol{\sigma} : \mathrm{sym}(\nabla \mathbf{v}) + \dot{e}]\, dV = 0 \tag{4.33}$$

Since the previous equality must hold for any arbitrary sub-body $\mathcal{S} \in \mathcal{B}$ the following identity must necessarily hold

$$\mathcal{D} = J\boldsymbol{\sigma} : \mathrm{sym}(\nabla \mathbf{v}) - \dot{e} \tag{4.34}$$

To conclude, the second principle of thermodynamics establishes that the dissipation is either zero or positive for any possible process. That is, $\mathcal{D} \geq 0$. This implies that

$$J\boldsymbol{\sigma} : \mathrm{sym}(\nabla \mathbf{v}) - \dot{e} \geq 0 \tag{4.35}$$

which is widely known as the Clausius-Duhem inequality. Recalling that $\boldsymbol{\tau} = J\boldsymbol{\sigma}$ is the Kirchhoff stress tensor and that $\mathbf{D} = \mathrm{sym}(\nabla \mathbf{v})$ its work conjugate, inequality 4.35 can be expressed in terms of other work conjugate pairs of stresses and strain rates. As an example, it can be expressed in terms of the Lagrangian (or Green) strain tensor rate $\dot{\mathbf{E}}$ and its work conjugate, the second Piola-Kirchhoff stress tensor $\mathbf{S}$

$$\mathbf{S} : \dot{\mathbf{E}} - \dot{e} \geq 0 \tag{4.36}$$

It is important to mention that in the following sections only isothermal processes for which the stored energy density e is the Helmholtz free energy will be considered. That is,

the Clausius-Duhem inequality for isothermal processes can be expressed as

$$\mathbf{S} : \dot{\mathbf{E}} - \dot{A} \geq 0 \tag{4.37}$$

where A represents the Helmholtz free energy. The constraint to focus on isothermal processes is not really a big limitation in multiphysics processes since the changes in temperature (or other non-local processes) can be addressed by the application of staggered procedures [51] [52] [53] [54] [55].

4.3.2 Coleman's method

Let us consider a generic isothermal process for which the Helmholtz free energy depends on the deformation of the material (some measure of it) and a given set of internal variables $\mathbf{q}$. Under these assumptions, Coleman's method provides a systematic tool to impose constraints to our constitutive relations based on the thermodynamic considerations exposed in the previous section.

For example, considering Green's strain tensor as such measure of deformation the following functional dependence for A is obtained

$$A = A(\mathbf{E}, \mathbf{q}) \tag{4.38}$$

Thus, its time derivative becomes

$$\dot{A} = \frac{\partial A}{\partial \mathbf{E}} : \dot{\mathbf{E}} + \frac{\partial A}{\partial \mathbf{q}} \cdot \dot{\mathbf{q}} \tag{4.39}$$

Inserting equation 4.39 into inequality 4.37 it becomes

$$\mathbf{S} : \dot{\mathbf{E}} - \frac{\partial A}{\partial \mathbf{E}} : \dot{\mathbf{E}} - \frac{\partial A}{\partial \mathbf{q}} \cdot \dot{\mathbf{q}} \geq 0 \tag{4.40}$$

which, after grouping terms can be expressed as

$$\left(\mathbf{S} - \frac{\partial A}{\partial \mathbf{E}} \right) : \dot{\mathbf{E}} - \frac{\partial A}{\partial \mathbf{q}} \cdot \dot{\mathbf{q}} \geq 0 \tag{4.41}$$

Coleman postulates that the term between parenthesis must vanish so that the inequality remains valid for all strain rates $\dot{\mathbf{E}}$. That is,

$$\mathbf{S} - \frac{\partial A}{\partial \mathbf{E}} = 0 \tag{4.42}$$

Under this condition, the expressions for the stress tensor as well as the dissipation can be derived exclusively from the Helmoltz free energy. That is,

$$\mathbf{S} = \frac{\partial A}{\partial \mathbf{E}} \quad , \quad \mathcal{D} = -\frac{\partial A}{\partial \mathbf{q}} \cdot \dot{\mathbf{q}} \geq 0 \tag{4.43}$$

where the equation on the right is often called reduced dissipation inequality.

4.4 Polycrystal model

Once the polycrystalline geometry has been generated by means of the procedure depicted in chapter 2, the mechanical response of the polycrystal is modeled.

The motion of the polycrystal in general, and each grain in particular, is governed by the equations of conservation of mass, linear and angular momentum. But these equations

alone are not enough to completely describe the mechanical response of the system as a constitutive response for the material must be adopted.

The step towards the creation of a model for the mechanical response of the polycrystal is to assume that each grain is conformed by a single crystal with a given random lattice orientation. Mathematically, each lattice orientation can be represented by means of a rotation $\mathbf{R}$ applied to a reference (or standard) lattice orientation.

Based on the previous assumptions, the problem is reduced, at the grain level, to the application of an elastic-plastic constitutive response. The details of the adopted crystal plasticity model as well as its numerical implementation are developed in the next subsection.

4.4.1 Single crystal plasticity model

In classical plasticity theory, the microscopic deformation mechanisms are not accounted for explicitly: they are lumped into macroscopic variables such as the plastic strain and shape of the yield surface. On the other hand, single crystal plasticity models move one step forward from those models by accounting explicitly for the material microstructure and mechanisms that lead to plastic deformation.

The origins of the theory date back to the pioneering work of Taylor [56] who was the first one to develop a continuum model of slip. His model is based on the realization that plastic deformation occurs in the form of smooth shearing on the slip planes and in the slip directions, with all of them depending on the particular lattice geometry.

Taylor's work was further extended to elastoplastic deformation with small elastic strains by Hill [57], and to the more general case of finite elastic-plastic deformations by Rice [58], Kratochvil [59], Hill and Rice [60], Havner [61], Asaro and Rice [62] and Hill and Havner [63]

among others.

4.4.1.1 Constitutive framework

For the purpose of this work, let us assume linearized kinematics. Within this context, $\mathbf{u}$ represents the displacement field the body under consideration. That is, the deformation mapping takes the form

$$\boldsymbol{\varphi}(\mathbf{X}) = \mathbf{X} + \mathbf{u}(\mathbf{X}), \quad \mathbf{X} \in \mathcal{B} \tag{4.44}$$

Under this assumption the linearized Green strain tensor becomes

$$\mathbf{E} \approx \frac{1}{2}\left(\nabla \mathbf{u} + \nabla \mathbf{u}^T\right) = \boldsymbol{\varepsilon} \tag{4.45}$$

whose conjugate stress is then the Cauchy stress tensor $\boldsymbol{\sigma}$. Thus, considering a Helmoltz free energy of the form $A = A(\boldsymbol{\varepsilon}, \gamma)$ where $\boldsymbol{\gamma}$ represents the set of active slips and applying Coleman's method the following expression is obtained:

$$\boldsymbol{\sigma} = \frac{\partial A}{\partial \boldsymbol{\varepsilon}} \quad , \quad \mathcal{D} = -\frac{\partial A}{\partial \boldsymbol{\gamma}} \cdot \dot{\boldsymbol{\gamma}} \geq 0 \tag{4.46}$$

It is common in finite plasticity to assume a multiplicative decomposition of the deformation gradient which can be expressed as

$$\mathbf{F} = \mathbf{F}^e \mathbf{F}^p \tag{4.47}$$

The linearization of the previous expression leads to the well known additive decompo-

sition of the strain tensor $\boldsymbol{\varepsilon}$ given by

$$\boldsymbol{\varepsilon} = \boldsymbol{\varepsilon}^e + \boldsymbol{\varepsilon}^p(\gamma) \tag{4.48}$$

where $\boldsymbol{\varepsilon}$, $\boldsymbol{\varepsilon}^e$ and $\boldsymbol{\varepsilon}^p$ are the linear parts of $\mathbf{F}$, $\mathbf{F}^e$ and $\mathbf{F}^p$ respectively. Furthermore, considering that the plastic deformation occurs in the form of smooth shearing on the slip planes and in the slip directions, the following kinematic constraint on the plastic strain tensor is imposed

$$\boldsymbol{\varepsilon}^p(\gamma) = \sum_{\alpha=1}^{N} \gamma^\alpha \mathrm{sym}(\mathbf{s}^\alpha \otimes \mathbf{m}^\alpha) \tag{4.49}$$

In the previous equation, $\mathbf{s}^\alpha$ and $\mathbf{m}^\alpha$ are orthogonal and define the slip direction and slip normal of the slip system α.

The deformation process in crystal plasticity can be thought of as a superposition of a long-range macroscopic field given by the elastic distortion of the lattice and a short-range microscopic field given by the presence of dislocations. This assumption, oftentimes referred to as structure-insensitive elastic response, allows a further simplification of the expression of the free energy [58] [64], which takes the form

$$A(\boldsymbol{\varepsilon}, \boldsymbol{\gamma}) = W^e(\boldsymbol{\varepsilon}, \boldsymbol{\varepsilon}^e(\boldsymbol{\gamma})) + W^p(\boldsymbol{\gamma}) \tag{4.50}$$

Under these assumptions, the expression for the Cauchy stress tensor can be further simplified:

$$\frac{\partial A}{\partial \boldsymbol{\varepsilon}} = \frac{\partial W^e}{\partial \boldsymbol{\varepsilon}} + \overbrace{\frac{\partial W^p}{\partial \boldsymbol{\varepsilon}}}^{\mathbf{0}} = \frac{\partial W^e}{\partial \boldsymbol{\varepsilon}^e} : \overbrace{\frac{\partial \boldsymbol{\varepsilon}^e}{\partial \boldsymbol{\varepsilon}}}^{\mathbf{I}} \quad \Rightarrow \quad \boldsymbol{\sigma} = \frac{\partial W^e}{\partial \boldsymbol{\varepsilon}^e} \tag{4.51}$$

Of particular interest are the forces conjugate to the plastic slips, which are given by

$$\mathbf{y} = -\frac{\partial A}{\partial \boldsymbol{\gamma}} = -\frac{\partial W^e}{\partial \boldsymbol{\gamma}} - \frac{\partial W^p}{\partial \boldsymbol{\gamma}} \tag{4.52}$$

For a given slip system α the following expression is obtained

$$\frac{\partial W^e}{\partial \gamma^\alpha} = \frac{\partial W^e}{\partial \boldsymbol{\varepsilon}^e} : \frac{\partial \boldsymbol{\varepsilon}^e}{\partial \gamma^\alpha} = -\boldsymbol{\sigma} : \mathrm{sym}(\mathbf{s}^\alpha \otimes \mathbf{m}^\alpha) = -\tau^\alpha \tag{4.53}$$

where τ^α is the resolved shear stress for the slip system α. As a consequence, the driving force $\mathbf{y}$ can be expressed as

$$y^\alpha = \tau^\alpha - \frac{\partial W^p}{\partial \boldsymbol{\gamma}^\alpha} \tag{4.54}$$

As can be seen, this is as far as one can go under the given general assumptions. Both the expressions for the stress and the force conjugate to the slip system α depend on the structure of the elastic and plastic contributions to the free energy.

Modeling the elastic response of the crystal as Hookean it takes the form

$$W^e = \boldsymbol{\varepsilon}^e : \mathbf{C}^e : \boldsymbol{\varepsilon}^e \tag{4.55}$$

where $\mathbf{C}^e$ is the fourth order tensor of elastic constants, which for the case of a cubic lattice (valid for both FCC and BCC crystals) rotated by $\mathbf{R}$ with respect to the standard orientation takes the form [65]

$$\mathbf{C}^e = \mathbf{R}^T \cdot \mathbf{R}^T \cdot \mathbf{C}_0 \cdot \mathbf{R} \cdot \mathbf{R} \tag{4.56}$$

where $\mathbf{C}_0$ can be expressed using Voigt notation as

$$\mathbf{C}_0 = \begin{bmatrix} C_{11} & C_{12} & C_{12} & 0 & 0 & 0 \\ C_{12} & C_{11} & C_{12} & 0 & 0 & 0 \\ C_{12} & C_{12} & C_{11} & 0 & 0 & 0 \\ 0 & 0 & 0 & C_{44} & 0 & 0 \\ 0 & 0 & 0 & 0 & C_{44} & 0 \\ 0 & 0 & 0 & 0 & 0 & C_{44} \end{bmatrix} \tag{4.57}$$

where the previous expressions, C_{11}, C_{12} and C_{44} are material constants. Thus, for Hookean materials, the expression for the Cauchy's stress reduces to $\boldsymbol{\sigma} = \mathbf{C}^e : \boldsymbol{\varepsilon}^e$.

On the other hand, one standard expression for the plastic contribution has the following form

$$W^p = \sum_{\alpha=1}^{N} \tau_0^\alpha \gamma^\alpha + \sum_{\alpha=1}^{N} \sum_{\beta=1}^{N} h_{\alpha\beta} \gamma^\alpha \gamma^\beta \tag{4.58}$$

where N is the number of slip systems, τ_0^α is the initial critical resolved shear stress for the system α, and $h_{\alpha\beta}$ is the hardening matrix of the crystal. Thus, the expression for the force conjugate to the plastic slip γ^α reduces to

$$y^\alpha = \tau^\alpha - \tau_c^\alpha \tag{4.59}$$

where τ_c^α is the critical resolved shear stress for the slip system α defined as

$$\tau_c^\alpha = \tau_0^\alpha + \sum_{\beta=1}^{N} h_{\alpha\beta} \gamma^\beta \tag{4.60}$$

Several models have been proposed for the determination of the hardening coefficients.

The most widely accepted are those proposed by Hutchinson [66], Pierce, Asaro and Needleman [67], Bassani and Wu [68], and Cuitino and Ortiz [69]. Note that for the case of ideal crystal plasticity the hardening coefficients $h_{\alpha\beta}$ vanish.

Within this context, the classical elements present in classical rate-independent plasticity theory can be formulated [65] [70].

The elastic domain $\mathcal{E}$ can be defined as the space generated by the stresses and slips such that the driving force is equal to zero or negative. Mathematically, it can be expressed as

$$\mathcal{E} = \{(\boldsymbol{\sigma}, \boldsymbol{\gamma}) \mid \tau^\alpha - \tau_c^\alpha \leq 0\} \tag{4.61}$$

where we adopted the notation $\boldsymbol{\gamma}$ to denote the vector composed by the slips corresponding to the different slip systems.

The collection of functions

$$f^\alpha(\boldsymbol{\sigma}, \tau_c^\alpha) = \tau^\alpha - \tau_c^\alpha \tag{4.62}$$

determines what in classical plasticity theory is referred to as the yield surface. In addition, the hardening law can be obtained by direct differentiation of equation 4.60

$$\dot{\tau}_c^\alpha = \sum_{\beta=1}^{N} h^{\alpha\beta}\dot{\gamma}^\beta \tag{4.63}$$

The rate of plastic deformation, or plastic strain evolution, is constrained by the kinematic assumption expressed in equation 4.49. That is,

$$\dot{\boldsymbol{\varepsilon}}^p = \sum_{\alpha=1}^{N} \dot{\gamma}^\alpha \mathrm{sym}\{\mathbf{s}^\alpha \otimes \mathbf{m}^\alpha\}, \quad \dot{\gamma}^\alpha \geq 0 \tag{4.64}$$

As in any plasticity problem, the stress must be admissible, i.e., must lie within the

elastic domain $\mathcal{E}$. In addition, it is required for the rate of plastic slip to be nonnegative. In particular, the plastic flow can only take place on the yield surface. These requirements are known as the the Kuhn-Tucker loading conditions [71] and can be summarized as

$$\dot{\gamma}^\alpha \geq 0, \quad f^\alpha(\boldsymbol{\sigma}, \tau_c^\alpha) \leq 0, \quad \dot{\gamma}^\alpha f^\alpha(\boldsymbol{\sigma}, \tau_c^\alpha) = 0 \tag{4.65}$$

4.4.1.2 Numerical implementation

As pointed out by Ortiz and Stainier [72], the internal-variable rates and flow rule for general viscoelastic materials can be derived from a variational principle which represents a generalization of the principle of maximum dissipation [70]. The discrete form of this variational principle leads to the so called variational update. Therefore, as a consequence of the potential structure of the update, the symmetry of the tangent stiffness matrix is guaranteed.

When applied to the crystal plasticity model developed in the previous section, the variational updates are equivalent to an optimal choice of active slip systems. Then, the minimization problem to consider takes the form

$$\min_{\gamma_{n+1}^\alpha} F\left(\gamma_{n+1}^\alpha; \boldsymbol{\varepsilon}_{n+1}, \boldsymbol{\varepsilon}_n^p, \gamma_n^\alpha\right) \quad \text{with} \quad \gamma_{n+1}^\alpha \geq \gamma_n^\alpha, \quad \alpha = 1, ..., N \tag{4.66}$$

where F can be expressed as

$$F\left(\gamma_{n+1}^\alpha; \boldsymbol{\varepsilon}_{n+1}, \boldsymbol{\varepsilon}_n^p, \gamma_n^\alpha\right) = W^e(\boldsymbol{\varepsilon}, \boldsymbol{\varepsilon}^e(\gamma_{n+1}^\alpha)) + W^p(\gamma_{n+1}^\alpha) \tag{4.67}$$

This problem can be addressed by standard nonlinear optimization algorithms such as the projected Newton method and sequential quadratic programming [73]. For the present

study, the simpler method proposed by Cuitino and Ortiz [69] is adopted. Basically, it resembles the projected Newton method for the case when the line search is avoided.

The procedure for determining the set of active slip systems $\mathcal{L}$ [69] is detailed in algorithm 5.

Algorithm 5: Determination of active slip systems.

Input: maximum iterations N

initialize $\mathcal{L} = \emptyset$;
for $(k = 0, ..., N)$ **do**
  compute $\Delta\gamma^\alpha$ based on current $\mathcal{L}$;
  if $(\Delta\gamma^\alpha < 0)$ **then**
    remove α from $\mathcal{L}$;
    $\Delta\gamma^\alpha \leftarrow 0$;
  if $(\tau^\alpha_{n+1} \leq \tau^\alpha_{c\,n+1} \;\; \forall\alpha \; not \; in \; \mathcal{L})$ **then**
    return $\mathcal{L}$;
  else
    $\mathcal{L} \leftarrow \arg\{\max[\tau^\alpha_{n+1} - \tau^\alpha_{c\,n+1}]\}$;
return `FAIL`;

4.4.2 Calibration for AISI 4340 steel

Since the interest of this thesis relies on the behavior of polycrystalline materials rather than single crystals, the calibration of the elastic-plastic material parameters was performed by simulating an axial tension test for a polycrystalline sample and fitting its response to the measured stress-strain curve for macroscopically tested AISI 4340 steels.

To avoid volumetric locking, grains have been discretized by means of tetragonal elements with enriched shape functions by inserting nodes on the faces, known as P2/P0loc elements (see figure 4.1).

Figure 4.2 shows the calibration of AISI 4340 alloy steel stress-strain response for two typical tensile curves obtained from [4].

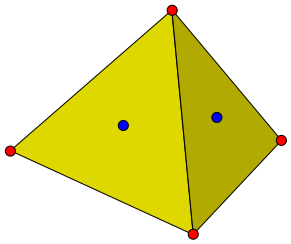

Figure 4.1: P2-P0loc element. The linear interpolation is enriched by inserting nodes on the barycenter of each face of the tetrahedron.

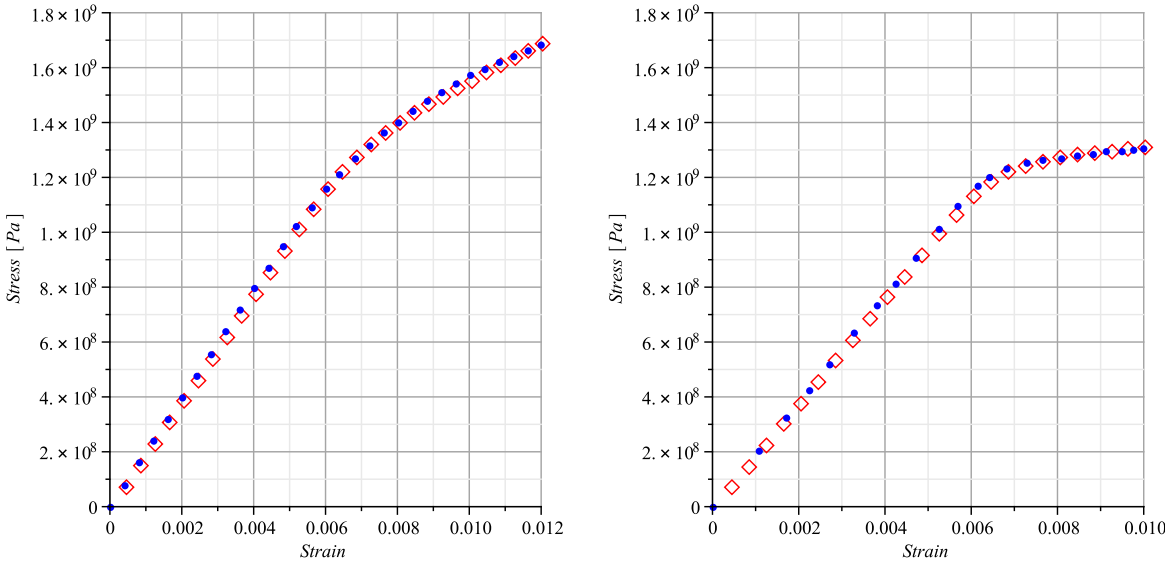

Figure 4.2: Calibration of AISI 4340 alloy steel stress-strain response for two typical tensile curves. (a) Ftu=1800 MPa and (b) Ftu=1380 MPa. The solids dots denote the experimental values [4] whereas the results obtained by direct numerical simulations of polycrystal are shown with diamond markers.

4.5 Intergranular cohesive fracture model

Having a model in place for the response of each grain in the polycrystal, it is now necessary to address the interaction between crystals at places where the intergranular fracture takes place. Thus, in order to achieve this goal, the classical cohesive theory of fracture is adopted.

The classical cohesive theory of fracture finds its origins in the pioneering works by Dugdale [74], Barenblatt [75] and Rice [76]. In this approach, fracture is regarded as a progressive phenomenon in which separation takes place across a cohesive zone ahead of the crack tip and is resisted by cohesive tractions.

Two main approaches have been proposed to implement the cohesive theory of fracture in finite element analysis: mixed boundary conditions [77] [78] [79] [80] [81] [82] [83] [84] [85] [86] and cohesive finite elements [87] [88] [89] [90] [53] [30]. In this thesis the latter approach is adopted, particularly the one proposed by Ortiz and Pandolfi [30].

Even though this approach would make possible to track the evolution of cracks in the polycrystal, it is still necessary to modify the cohesive law to account for the effect of impurity segregation. A typical behavior under the presence of impurities is captured in the articles by Yamaguchi et al. [12] and Jiang and Carter [5]. In the present work, the methodology introduced by Serebrinsky et al. [22] to include such effects in the cohesive element formulation is adopted.

4.5.1 Cohesive law

As in previous sections, let us consider the deformation of a body occupying a domain $\mathcal{B} \in \mathbb{R}^3$ in a certain reference configuration. The body undergoes a deformation determined by a mapping $\boldsymbol{\varphi}$. Furthermore, let us consider a sub-body $\mathcal{S} \in \mathcal{B}$ containing a cohesive surface $\mathcal{C}$ which divides $\mathcal{S}$ into $\mathcal{S}^+$ and $\mathcal{S}^-$ (see figure 4.3). Let us identify the corresponding sides

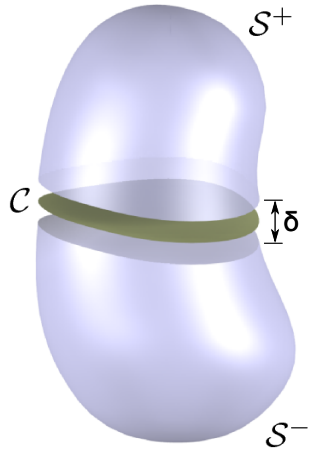

Figure 4.3: Body with cohesive surface.

of $\mathcal{C}$ as $\mathcal{C}^{\pm}$. Let $\mathbf{n}$ be the field of vectors normal to $\mathcal{C}$.

Following the notation previously used, the external power of the forces acting on $\mathcal{S}$ can be expressed as

$$P_{ext} = \sum_{\pm} \int_{\partial\boldsymbol{\varphi}(\mathcal{S}^{\pm})} \mathbf{t} \cdot \mathbf{v}\, da + \sum_{\pm} \int_{\boldsymbol{\varphi}(\mathcal{S}^{\pm})} \rho\mathbf{b} \cdot \mathbf{v}\, dv \tag{4.68}$$

where $\varphi(\mathcal{S}^{\pm})$ are the two bodies generated due to the presence of the cohesive surface. Analogously, the kinetic energy is given by

$$K = \sum_{\pm} \int_{\boldsymbol{\varphi}(\mathcal{S}^{\pm})} \left(\frac{1}{2}\rho\mathbf{v} \cdot \mathbf{v}\right) dv \tag{4.69}$$

On the other hand, the equilibrium relations can be expressed as

$$\operatorname{div}(\boldsymbol{\sigma}) + \rho\mathbf{b} = \rho\mathbf{a} \quad \text{in } \mathcal{S} \in \mathcal{B} \tag{4.70}$$

$$\mathbf{t} = \boldsymbol{\sigma} \cdot \mathbf{n} \quad \text{on } \partial\mathcal{S}^{\pm} \tag{4.71}$$

$$[\![\mathbf{t}]\!] = \mathbf{t}^{+} - \mathbf{t}^{-} = \mathbf{0} \quad \text{on } \mathcal{C}^{\pm} \tag{4.72}$$

By following a procedure similar to the one presented in section 4.3, applying Cauchy's tetrahedron theorem, considering the symmetry of $\boldsymbol{\sigma}$, taking advantage of the divergence theorem and considering conservation of linear momentum, the following expression for the deformation power identity is obtained:

$$P_{def} = P_{ext} - \dot{K} = \sum_{\pm} \int_{\boldsymbol{\varphi}(\mathcal{S}^{\pm})} \boldsymbol{\sigma} \cdot \mathrm{sym}(\nabla \mathbf{v}) \; dv + \int_{\varphi(\mathcal{C})} \mathbf{t} \cdot [\![\mathbf{v}]\!] \; da \tag{4.73}$$

As it can be seen on the previous equation, the presence of a cohesive surface results in the addition of a new term to the deformation power identity. This term can be interpreted as the work done by the tractions $\mathbf{t}$ on the displacement jumps $\boldsymbol{\delta} = [\![\boldsymbol{\varphi}]\!]$. According to Ortiz and Pandolfi [30], this work-conjugacy suggests the framework for the development of a general cohesive theory in solids where the opening displacements $\boldsymbol{\delta}$ play the role of a deformation measure and the tractions $\mathbf{t}$ play the role of conjugate stress measure.

Within this framework, Coleman's method can be applied where we postulate the existence of a free energy density per unit undeformed area over $\mathcal{C}$ of the general form

$$A = A(\boldsymbol{\delta}, \theta, c, \mathbf{q}; \nabla_{\mathcal{C}} \bar{\boldsymbol{\varphi}}) \tag{4.74}$$

where θ is the local temperature, c the impurity concentration on the cohesive surface, $\mathbf{q}$ represents internal variables and $\nabla_{\mathcal{C}} \bar{\boldsymbol{\varphi}}$ is a geometrical term representing the deformation of the mid-surface $\bar{\boldsymbol{\varphi}}$ given by

$$\bar{\boldsymbol{\varphi}} = \frac{1}{2}(\boldsymbol{\varphi}^{+} + \boldsymbol{\varphi}^{-}) \tag{4.75}$$

As in previous sections of this chapter, the multi-physics aspects of the problem are addressed by recourse to a staggered procedure. Thus, the temperature θ and the concen-

tration c (both non-local variables governed by a diffusion equation) are considered to hold constant at known values. Under this assumption, the free energy can be further simplified:

$$A = A(\boldsymbol{\delta}, \mathbf{q}; \nabla_{\mathcal{C}} \bar{\boldsymbol{\varphi}}) \tag{4.76}$$

An even simpler expression for the free energy can be obtained by assuming that the cohesive surface is isotropic and that the cohesive response is independent of the stretching and shearing of the cohesive surface. If, in addition, the restrictions imposed by material frame indifference are considered, the free energy density becomes

$$A = A(\delta_n, \delta_s, \mathbf{q}) \tag{4.77}$$

where δ_n and δ_s are the normal and tangential components of $\boldsymbol{\delta}$ respectively. Furthermore, with the introduction of the effective opening displacement

$$\delta = \sqrt{\beta^2 \delta_s^2 + \delta_n^2} \tag{4.78}$$

where β is a weighting factor for the sliding and normal opening displacements, the potential reduces to

$$A = A(\delta, \mathbf{q}) \tag{4.79}$$

Under all these assumptions, following Coleman's method, the cohesive law reduces to

$$\mathbf{t} = \frac{t}{\delta}(\beta^2 \boldsymbol{\delta}_s + \delta_n \mathbf{n}) \tag{4.80}$$

where

$$t = \frac{\partial A}{\partial \delta}(\delta, \mathbf{q}) \tag{4.81}$$

A commonly adopted expression for the free energy is the one corresponding to the Smith and Ferrante's universal binding law, which for the reversible case takes the form

$$A(\delta) = e\sigma_c\delta_c \left[1 - \left(1 + \frac{\delta}{\delta_c}\right) e^{-\frac{\delta}{\delta_c}}\right] \tag{4.82}$$

where $e \approx 2.71828$ is the e-number, δ_c is a characteristic open displacement and σ_c is the maximum cohesive normal traction. The traction t obtained from differentiation of the previous expression is, then

$$t = e\sigma_c \frac{\delta}{\delta_c} e^{-\frac{\delta}{\delta_c}} \tag{4.83}$$

4.5.2 Cohesive elements

The implementation of the cohesive law into a finite element analysis is performed by embedding it into surface-like finite elements, usually referred to as cohesive elements. Following Ortiz and Pandolfi [30], the proposed elements consists of two triangular surfaces, which coincide in space in the reference configuration. Each surface has n-nodes, depending on the adopted interpolation scheme. Therefore, each cohesive element is composed by $2n$-nodes.

Let us denote by $p_a(s_1, s_2)$, $a = 1, ..., n$ the standard shape functions of the constituent surface elements, where the (s_1, s_2) represent the natural coordinates of each surface in some standard configuration.

For the model developed in the previous section, the cohesive tractions per unit reference area are

$$\mathbf{t} = \frac{t}{\delta}[\beta^2\boldsymbol{\delta} + (1 - \beta^2)(\boldsymbol{\delta} \cdot \mathbf{n})\mathbf{n}] \tag{4.84}$$

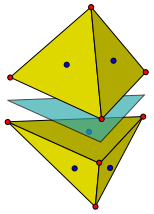

Figure 4.4: 4-node cohesive element.

Furthermore, the cohesive nodal forces follow from the tractions as

$$f_{ia}^{\pm} = \mp \int_{\mathcal{C}} t_i p_a \, dA \tag{4.85}$$

The tangent stiffness matrix corresponding to the cohesive element can be obtained by inserting equation 4.84 into 4.85 and linearizing the resulting expression. Thus, the following expression is obtained

$$K_{iakb}^{\pm\pm} = \int_{\mathcal{C}} \frac{\partial f_{ia}^{\pm}}{\partial x_{kb}^{\pm}} \, dA = \mp \mp \int_{\mathcal{C}} \frac{\partial t_i}{\partial \delta_k} p_a p_b \, dA \mp \frac{1}{2} \int_{\mathcal{C}} \frac{\partial t_i}{\partial n_p} \frac{\partial n_p}{\partial \bar{x}_{kb}} p_a \, dA \tag{4.86}$$

This study only considers linearized kinematics. Therefore, the geometric terms in equation 4.86 vanish resulting in

$$K_{iakb}^{\pm\pm} = \mp \mp \int_{\mathcal{C}} \frac{\partial t_i}{\partial \delta_k} p_a p_b \, dA \tag{4.87}$$

For the purposes of the present work, triangular cohesive elements with a node in the barycenter were adopted to ensure compatibility with the solid P2-P0loc elements (see figure 4.4).

Table 4.1: Summary of studies that show impurity-enhanced decohesion

Authors	**System**	**Technique**
Heuer et al. [13]	S in Ni	Experimental
van der Ven and Ceder [91]	H in Al; O in Al	First principles
Jiang and Carter [5]	H in Fe; H in Al	First principles
Krupp et al. [15]	O in Ni	Experimental
Yamaguchi et al. [12]	S in Ni	First principles
Lu et al. [92]	Na in Al; Ca in Al	First principles & exp.
Zhang et al. [93]	Ga in Al	First principles
Yamaguchi et al. [14]	S in Fe; P in Fe	First principles
Yamaguchi and Kaburaki [21]	O in Fe; O in Ni	First principles
Zhang et al. [94]	S in Al	First principles

4.5.3 Effect of impurity concentration

As mentioned before, even though the previous approach would make possible to track the evolution of cracks in the polycrystal, it is still necessary to modify the cohesive law in order to account for the effect of impurity segregation on the grain boundaries.

It is widely known that impurity segregation on grain boundaries of polycrystalline metals can induce intergranular embrittlement. This phenomenon is usually referred to as impurity-enhanced decohesion, and as mentioned in the introductory chapter of this thesis, it is of great importance in technological applications.

Several research efforts, some of which have been summarized in table 4.1, have attempted to explain and understand the underlying mechanisms of this intergranular embrittlement.

A representative example of this effort is the work by Yamaguchi et al. [12], where they try to address why and how sulfur weakens the grain boundaries of nickel by means of first principles computations. The authors found that a short-range overlap repulsion among densely segregated and neighboring sulfur atoms causes a large grain boundary expansion, and that this expansion facilitates the grain boundary decohesion. As a result, the grain

boundary tensile strength is reduced by one order of magnitude. Their results are in good agreement with the experimental findings of Heuer et al. [13].

In a recent article, Yamaguchi [14] extended his work to study the decohesion of ferromagnetic BCC iron grain boundaries by sulfur or phosphorous segregation. As a result, the authors found two main embrittlement mechanisms which prevail at different extents for different impurity elements. The main mechanism for the sulfur-induced decohesion is fracture surface stabilization with reference to the grain boundary by the segregated solute atoms without interaction between them. In the case of phosphorous-induced embrittlement, the predominant mechanism is grain boundary destabilization by a repulsive interaction among the segregated and neighboring solute atoms. This difference in the predominant decohesion mechanism makes sulfur a much stronger embrittling element than phosphorous.

Another interesting work is the one performed by Krupp et al. [15] on oxygen-induced intergranular fracture of the nickel-base alloy IN718 during mechanical loading at high temperatures. This nickel-based superalloy, commonly used in high-temperature high-strength components in gas turbines, exhibits a change in the failure mechanism when loaded slowly at temperatures above 600^{o} C. It has been observed that the cycle-dependent fatigue failure gives place to a time-dependent intergranular brittle fracture [16] [17] [18] [19] [20]. Even though several authors have attributed this transition to grain boundary oxidation, one of the principal findings of their experimental study is that oxygen-induced intergranular fracture does not necessarily requires the formation of oxides. Furthermore, their work suggest that oxygen-enhanced decohesion might be the predominant mechanism of intergranular fracture at high temperature.

Krupp's hypothesis is supported by first-principles calculations performed by Yamaguchi and Kaburaki [21]. They found that the formation energy of NiO per oxygen atom is larger

than or comparable to the grain boundary segregation energy of oxygen. Furthermore, their findings show that oxygen has a strong embrittlement effect when segregated to the grain boundary.

Despite the nature of the predominant decohesion mechanism for a given system, it is clear that the presence of impurities may have a strong embrittlement effect on the grain boundary cohesive energy. This is precisely the effect our model intends to capture. Towards this end, the methodology introduced by Serebrinsky et al. [22] for modeling hydrogen embrittlement is followed.

Let us define the impurity coverage θ in terms of the impurity concentration at the grain boundary c as

$$\theta = \frac{c}{c + \exp\left(\frac{-\Delta g_b^0}{RT}\right)} \tag{4.88}$$

where Δg_b^0 is the free energy difference between the adsorbed and bulk standard states, R the gas constant and T the temperature. As seen before, the cohesive free energy depends on two parameters namely δ_c and σ_c. Therefore, a change in the cohesive energy as a function of the impurity coverage θ could be achieved through a dependence of δ_c or σ_c on θ.

The calculations of van der Ven and Ceder [91] show that δ_c is insensitive to the coverage for hydrogen in aluminum. Thus, in order to simplify the approach presented in this thesis, it is assumed that the embrittlement effect is a result of a dependence of σ_c on θ. That is, the cohesive energy for the embrittled material can be expressed as

$$2\gamma(\theta) = \int_0^\infty e\sigma_c(\theta)\frac{\delta}{\delta_c}e^{-\frac{\delta}{\delta_c}}\,d\delta = e\delta_c\sigma_c(\theta) \tag{4.89}$$

On the other hand, it is possible to obtain the dependence of the cohesive energy on

impurity coverage from first principles computations [5]. Then, let us assume that the ratio $\gamma(\theta)/\gamma_{ref}$ is given, where γ_{ref} is the reference value for null coverage. Therefore, from equation 4.89 the following expression is obtained

$$\sigma_c(\theta) = \left(\frac{\gamma(\theta)}{\gamma_{ref}}\right)\sigma_{ref} \tag{4.90}$$

where σ_{ref} is the maximum cohesive traction under absence of impurities. Consequently, the traction-separation law takes the form

$$t(\delta,\theta) = e\frac{\delta}{\delta_c}\left(\frac{\gamma(\theta)}{\gamma_{ref}}\right)\sigma_{ref}e^{-\frac{\delta}{\delta_c}} \tag{4.91}$$

Equation 4.91 provides a coupling between the grain boundary diffusion model developed in chapter 3 and the mechanical models elaborated in the present chapter.

Figure 4.5 shows the hydrogen embrittlement effect on iron as reported in [5]. Figure 4.6 shows the cohesive law for several values of impurity coverage, taking the dependence on θ from [22].

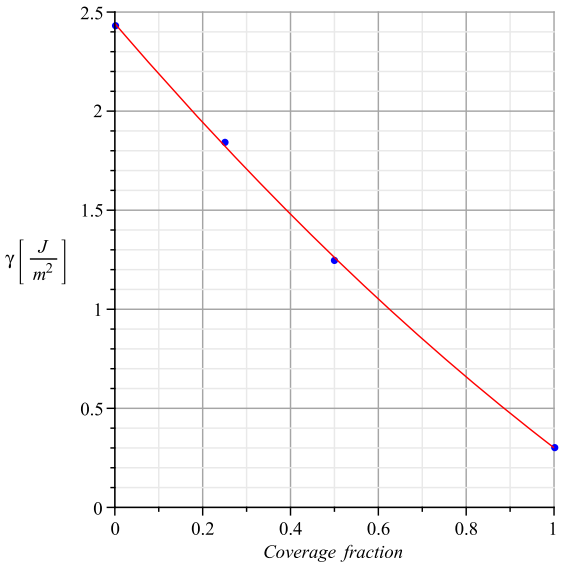

Figure 4.5: Effect of hydrogen on cohesive energy of bcc Fe(1 1 0). First principles computations [5] (solid circles) and quadratic fit (line).

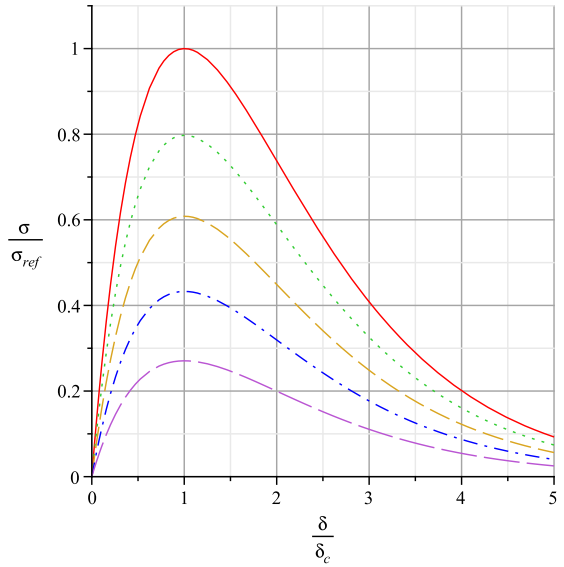

Figure 4.6: Traction-reparation law for different values of impurity coverage for H in Fe: $\theta = 0.0$ (solid), $\theta = 0.2$ (dot), $\theta = 0.4$ (dash), $\theta = 0.6$ (dash-dot) and $\theta = 0.8$ (long dash)

Chapter 5

Validation and results

5.1 Introduction

At this point, all the features of the model for intergranular impurity-enhanced decohesion on polycrystals have been stated. The first section of this chapter will describe the salient features of the computer implementation of the model into a single computer program and discuss the adopted solution procedure. On the following section the focus will shift to the validation of the model by comparing simulation results against initiation time and crack-growth-rate tests for hydrogen embrittlement of AISI 4340 steel.

5.2 Computer implementation and solution procedure

All the models described in this work have been programmed into a computer code implemented in C++. The code was designed by having in mind the type of tests required to validate the model: crack nucleation (initiation time) and crack-growth-rate tests performed on compact specimens.

The compact test specimens are usually machined from plates which are cut from hot rolled round bars. Then, all specimens are generally electropolished and their surfaces (except the notch region) are coated with paint to avoid hydrogen diffusion from places

other than the notch roots.

In initiation time tests, the specimen is loaded and the crack nucleation time is usually measured by the electrical potential method. A constant current is usually applied to the specimen and the voltage difference through the notch mouth is measured. The tests are interrupted and the time is recorded when an increase in the potential due to the presence of the crack is observed.

In crack-growth-rate tests, the specimen is loaded and the crack length is measured by a traveling microscope. In addition, a clip gage is sometimes mounted to detect the macroscopic growth behavior with higher sensitivity. The crack-growth-rate (velocity) is then computed numerically from the crack length history.

The computer code was devised in such a way that one simulation can be employed to measure both the initiation time and the crack-growth-rate as a function of the applied stress intensity factor.

Conceptually, the program execution can be divided in two main stages: (i) test initialization and (ii) temporal evolution. During the initialization stage, the geometry is generated and the boundary conditions for the diffusion problem are imposed. Afterwards, the cohesive law is updated to reflect the given impurity concentration distribution across the specimen. Finally, the mechanical pre-load is imposed incrementally until the desired stress intensity factor is reached.

The temporal evolution stage addresses the multiphysics aspects of the model by adopting a staggered procedure [95]. After computing the diffusion step, the impurity concentration is interpolated from the nodal values at the diffusion elements to the quadrature points of the cohesive elements. At those points, the cohesive law is then updated accordingly with the procedure described in chapter 4. Afterwards, the mechanical step solves the quasistatic

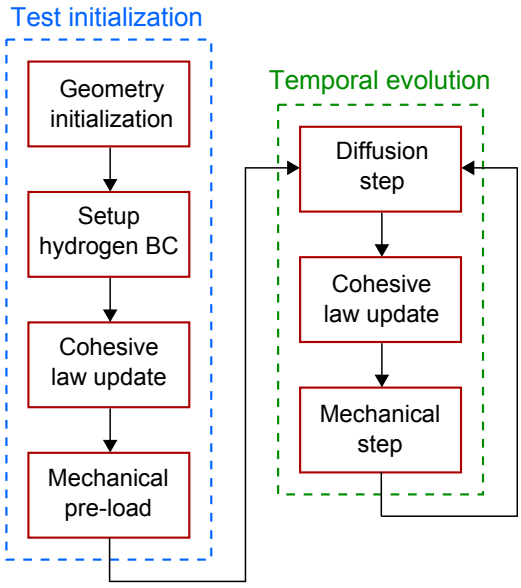

Figure 5.1: Staggered solution procedure.

equilibrium problem by means of the Newton-Raphson algorithm. Just before a discontinuous crack propagation occurs, the stiffness matrix becomes singular making necessary to use an alternative solver. When this is the case, the program searches for the static solution by means of dynamic relaxation, which is a much slower algorithm but very robust.

A schematic representation of the solution procedure and program organization is shown in figure 5.1.

5.3 Validation: hydrogen embrittlement of AISI 4340 steel

Stress corrosion cracking of high strength steels in aqueous solutions is generally recognized as hydrogen assisted cracking [96]. To validate our model, simulations of hydrogen embrittlement of AISI 4340 steel were performed and the obtained results compared to experimental data obtained from initiation time tests [6] and crack-growth-rate tests [7].

The complexity of the problem being addressed and its associated high computational

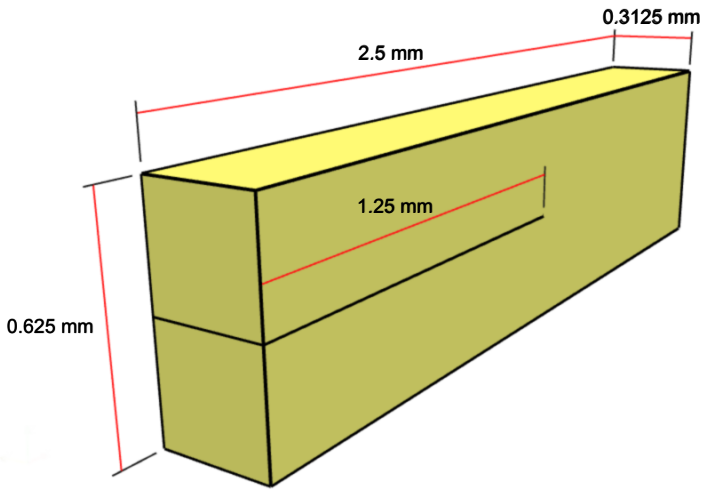

Figure 5.2: Geometry of the specimen considered in our simulations.

cost prevent us from simulating a specimen of identical dimensions to the specimens employed for the experiments. The geometry and dimensions of the modeled specimen are shown in figure 5.2.

In addition to modeling a specimen of small dimensions, the mesh was optimized in such a way that the grains have the desired size in the crack-propagating region but maintaining a coarser mesh away from the crack. Furthermore, different mesh regions were defined as shown in figure 5.3. Hookean isotropic material without plasticity requires much less computational power than its cubic symmetry counterpart, and the latter without plasticity is very light when compared to the case when crystal plasticity is present.

Due to all these optimizations, it was possible to simulate a model with 600 grains in the region of interest: 300 with cubic symmetry and no plasticity and 300 contemplating the crystal plasticity effect. The mechanical model has over 80,000 tetrahedral elements and 300,000 degrees of freedom. The diffusion model has only 12,000 degrees of freedom and the computational time required by it is negligible when compared to the cost of finding the mechanical equilibrium.

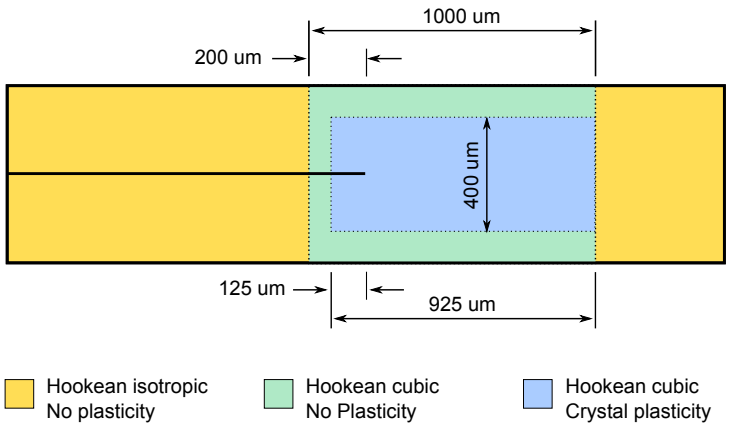

Figure 5.3: Mesh regions.

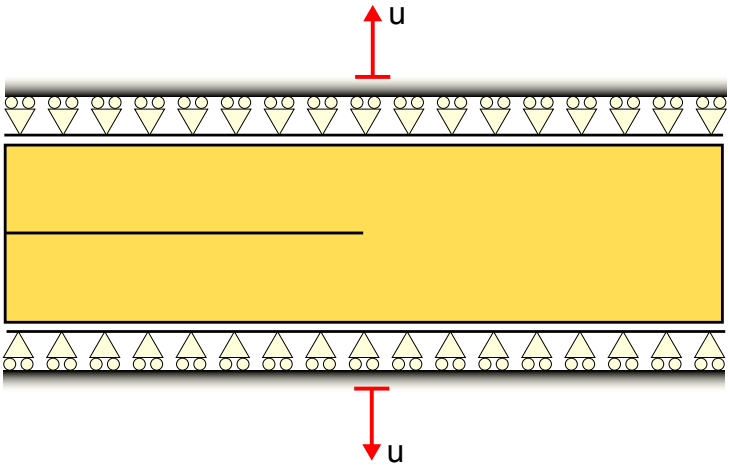

Figure 5.4: Mechanical boundary conditions.

To obtain a more stable simulation from the numerical point of view, the loading was implemented through the application of a controlled displacement to the upper and lower faces of the specimen. The applied boundary conditions for the mechanical problem are shown on figure 5.4. For the diffusion problem, a constant hydrogen coverage was prescribed on the pre-cracked region starting from the crack tip until 200 μm from it.

In order to compare the simulation results with the experiments, the stress intensity factor and the crack length had to be measured. The computational measurement of the stress intensity factor is not straightforward for the case being considered. For instance, the

well known J-integral cannot be evaluated due to the following factors:

1. The crack does not remain planar due to its intergranular nature.

2. The constitutive response of the material is highly nonlinear due to the presence of crystal plasticity.

3. The material presents cubic symmetry (anisotropic).

4. The sample is highly heterogeneous due to the random grain orientations.

Thus, a simplified approach was adopted. A specimen with mesh and dimensions identical to those of the one employed in the simulations but with isotropic Hookean material response without plasticity was loaded and the corresponding strain energy W measured. Then, the crack length was slightly changed in increments ds repeating the same procedure until four measurements W_1, W_2, W_3 and W_4 were obtained. Let b be the specimen width. The energy release rate is then given by

$$G = -\frac{1}{b}\frac{dW}{ds} \tag{5.1}$$

Its value was estimated employing the numerical derivative

$$\frac{dW}{ds} = \frac{1}{12 \cdot ds}\left(-W_4 + 8W_3 - 8W_2 + W_1\right) \tag{5.2}$$

Assuming plane strain conditions the applied stress intensity factor is given by

$$K_I = \frac{G \cdot E}{1 - \nu^2} \tag{5.3}$$

where E and ν are the homogeneous material properties. Assuming proportionality between

K_I and the applied displacement, the proportionality constant was computed and employed in the simulations for estimating the applied stress intensity factor.

On the other hand, the crack length was estimated as follows. First, the surface for which the cohesive opening is larger than the cohesive parameter δ_c was extracted for a given time t_n. Second, its area A_n was computed. Therefore, the crack length L_n was estimated as

$$L_n = \frac{A_n}{b} \tag{5.4}$$

The same procedure was performed for all recorded time steps obtaining in this way the crack length evolution as a function of time. The crack-growth rate was then obtained as the slope of the linear fit for the computed time history.

The elastic and plastic material properties were obtained by fitting their value to the uniaxial traction test as depicted in figure 4.2 (a) and the grain boundary diffusion constant was obtained following the procedure described in chapter 3. The average grain size was adopted in agreement with the experimental measures for hydrogen embrittlement of AISI 4340 steel reported in [97].

The material properties employed in the simulations are summarized in table 5.1. The main results gathered from our simulations, namely, crack growth, initiation time and crack-growth-rate, are summarized and discussed in the following sub sections.

5.3.1 Crack growth results

The obtained crack length as a function of time is plotted in figure 5.5 for applied stress intensity factors ranging from 13.7 to 41.2 $MPa\ \sqrt{m}$. It can be observed that the crack-growth-rate increases as the applied stress intensity factor gets larger. It is difficult though to appreciate other features of the simulations when plotting all of the results together as

Table 5.1: Material properties

Property	**Value**
Crystal structure	BCC
Slip planes	{321}
Slip directions	$< \bar{1}11 >$
# of slip systems	24
Grain size	$\approx 100 \mu m$
C_{11}	208.9 GPa
C_{12}	126.4 GPa
C_{14}	97.7 GPa
τ_c	570.0 MPa
C	171.0 MPa
r_0	0.01
m	0.80
K_{Ic}	58.4 $MPa\ \sqrt{m}$
D_{gb}	$2.53 \cdot 10^{-9}\ m^2/sec$

the time scale involved varies considerably for each of them.

Figure 5.6 shows, in different time scales, the results for applied stress intensity factors of 13.7 (a), 17.2 (b) and 37.8 (c) $MPa\ \sqrt{m}$. Each of the cases exhibit different features.

For $K_I = 13.7 MPa\ \sqrt{m}$ (figure 5.6a) the crack growth is mostly continuous and it is impossible just from analyzing the figure to tell apart crack initiation from crack propagation.

For the next computed loading level, the applied stress intensity factor takes the value 13.7 $MPa\ \sqrt{m}$ (figure 5.6b). In this case, the crack exhibits a continuous growth as well but a clear distinction between crack initiation and growth is evidenced by the presence of two regimes with different slopes.

For the remaining computed loading levels (20.6, 24.0, 27.5, 30.1, 34.3, 37.8 and 41.2 $MPa\ \sqrt{m}$) the observed behavior is identical to the one shown in figure 5.6c. First of all, there is a clear distinction between crack nucleation and crack propagation. The time for which the transition from one regime to the other occurs is what we refer to as initiation

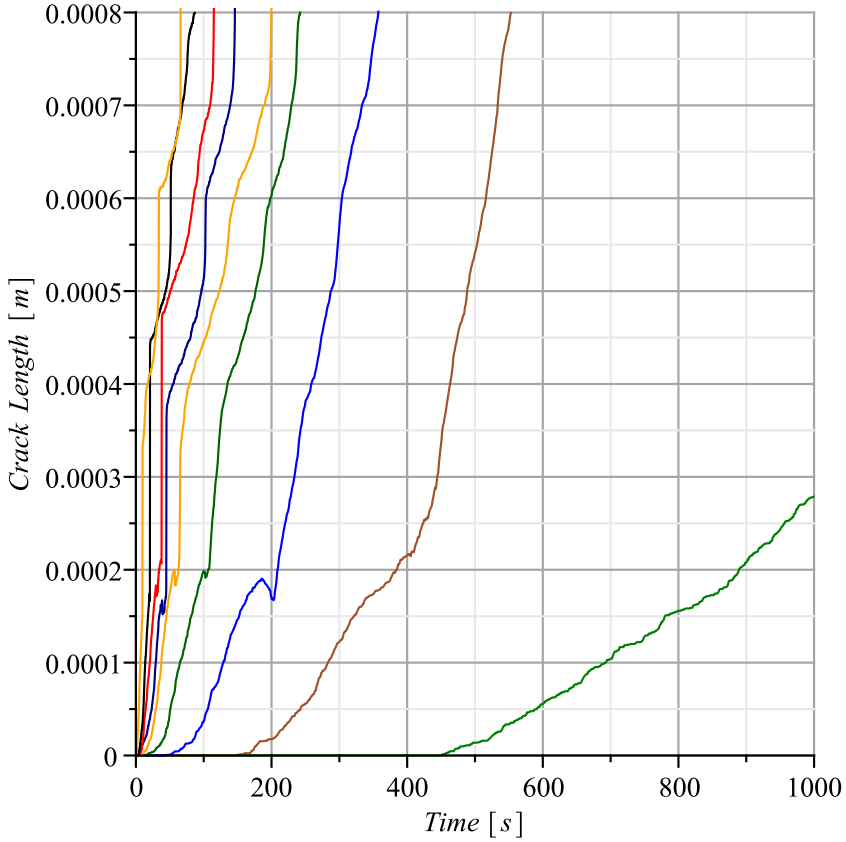

Figure 5.5: Crack length evolution for applied stress intensity factors ranging from 13.7 to 41.2 $MPa\ \sqrt{m}$.

time. It is observed that for all of these cases the transition occurs when the estimated crack length reaches 200 μm approximately. This value is roughly twice the average grain size for the simulation. Remarkably, the crack propagation stage is characterized by an intermittent crack growth indicated by jumps in the crack length in agreement with experimental observations [7]. These jumps have approximately the same magnitude within a given stress intensity factor. Nevertheless, the first jump, which indicates the transition from one regime to another, is considerably larger than the following ones.

Computations for loading levels above 41.2 $MPa\ \sqrt{m}$ were not possible to perform since the initiation jump length exceeded the size of the zone where cohesive elements were placed rendering the results invalid.

Figure 5.7 shows the temporal evolution of hydrogen coverage across the grain boundaries. Figure 5.8 and 5.9 show the temporal evolution of the crack in the specimen. In figure 5.8 the crack surface is shown in light blue whereas the contour levels represent the hydrogen coverage on the grain boundaries. Figure 5.9 shows the effective plastic strain in the regions surrounding the crack. All figures were computed for applied stress intensity factor $K_I = 41.2MPa\ \sqrt{m}$.

5.3.2 Initiation time results

The initiation time was identified for almost all of the loading levels as the time when the transition from the nucleation stage to the crack propagation stage occurs. As previously stated, this point occurs for most of the cases (stress intensity factors 20.6, 24.0, 27.5, 30.1, 34.3, 37.8 and 41.2 $MPa\ \sqrt{m}$) when the estimated crack length reaches 200 μm approximately. For the case when $K_I = 17.7$ it was adopted as the time for which a change in the growth slope was evidenced. Finally, for the lowest loading level where $K_I = 13.7$

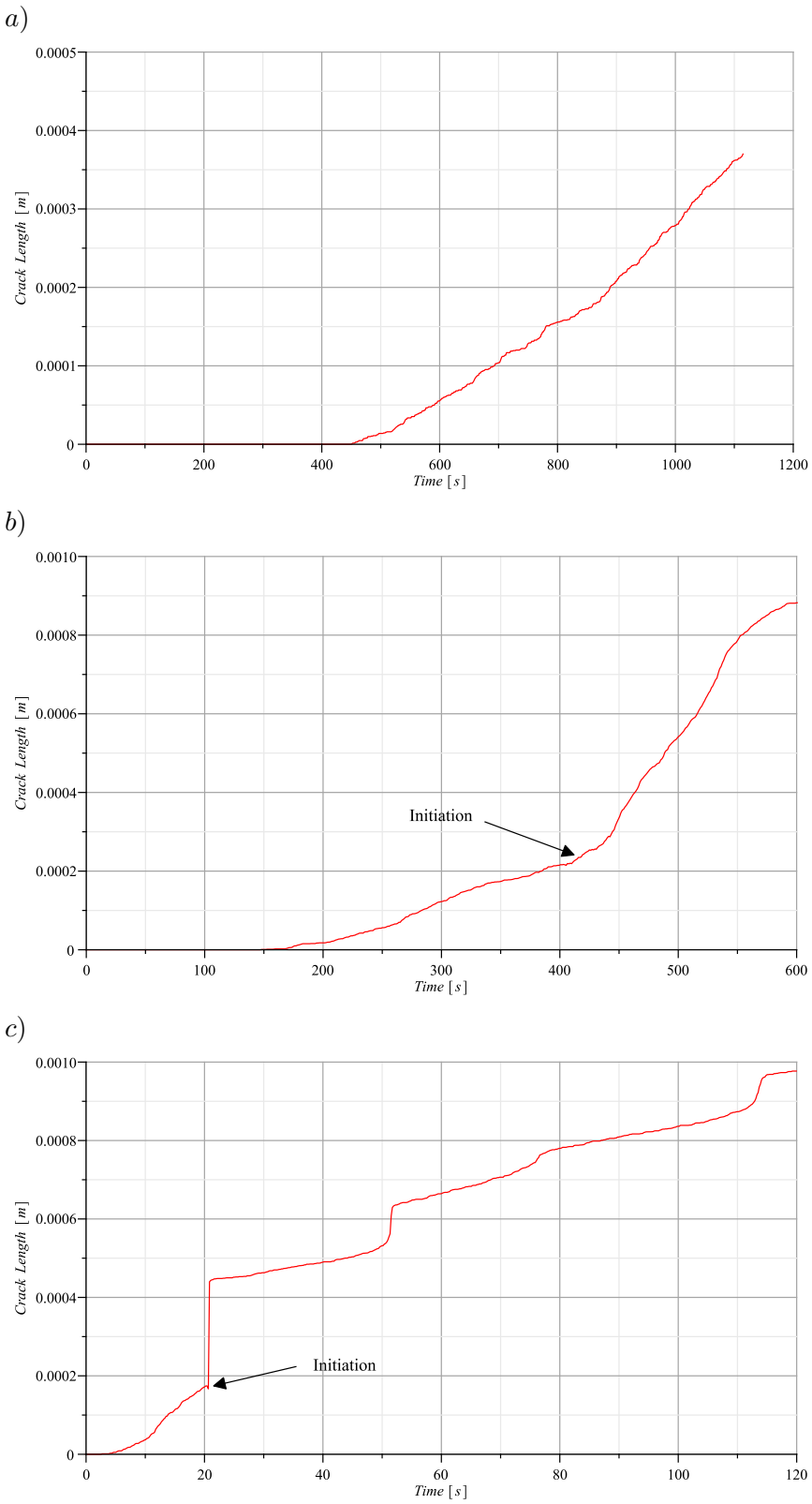

Figure 5.6: Crack length evolution for applied stress intensity factors 13.7 (a), 17.2 (b) and 37.8 (c) $MPa\ \sqrt{m}$.

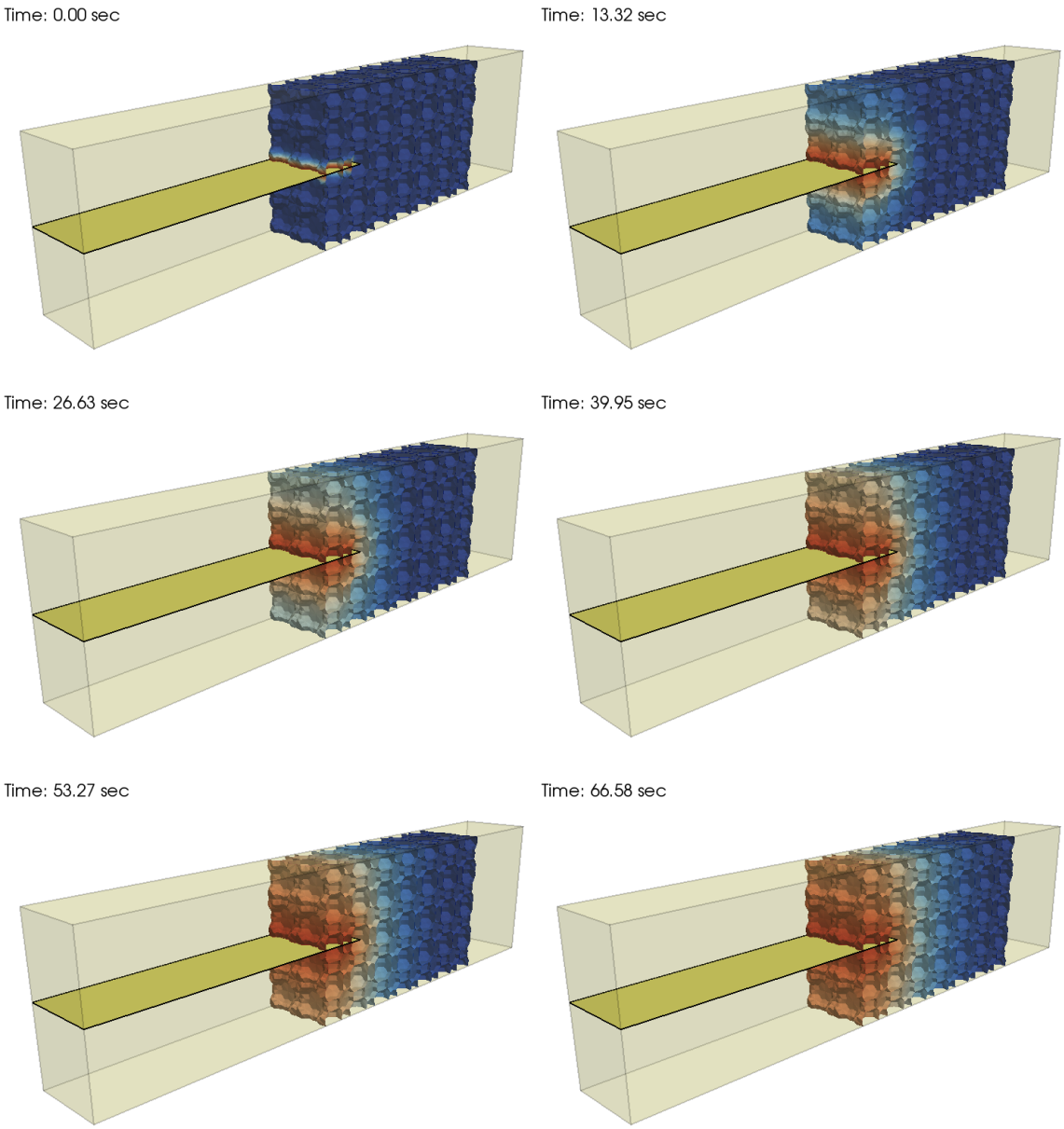

Figure 5.7: Temporal evolution of hydrogen coverage across the grain boundaries.

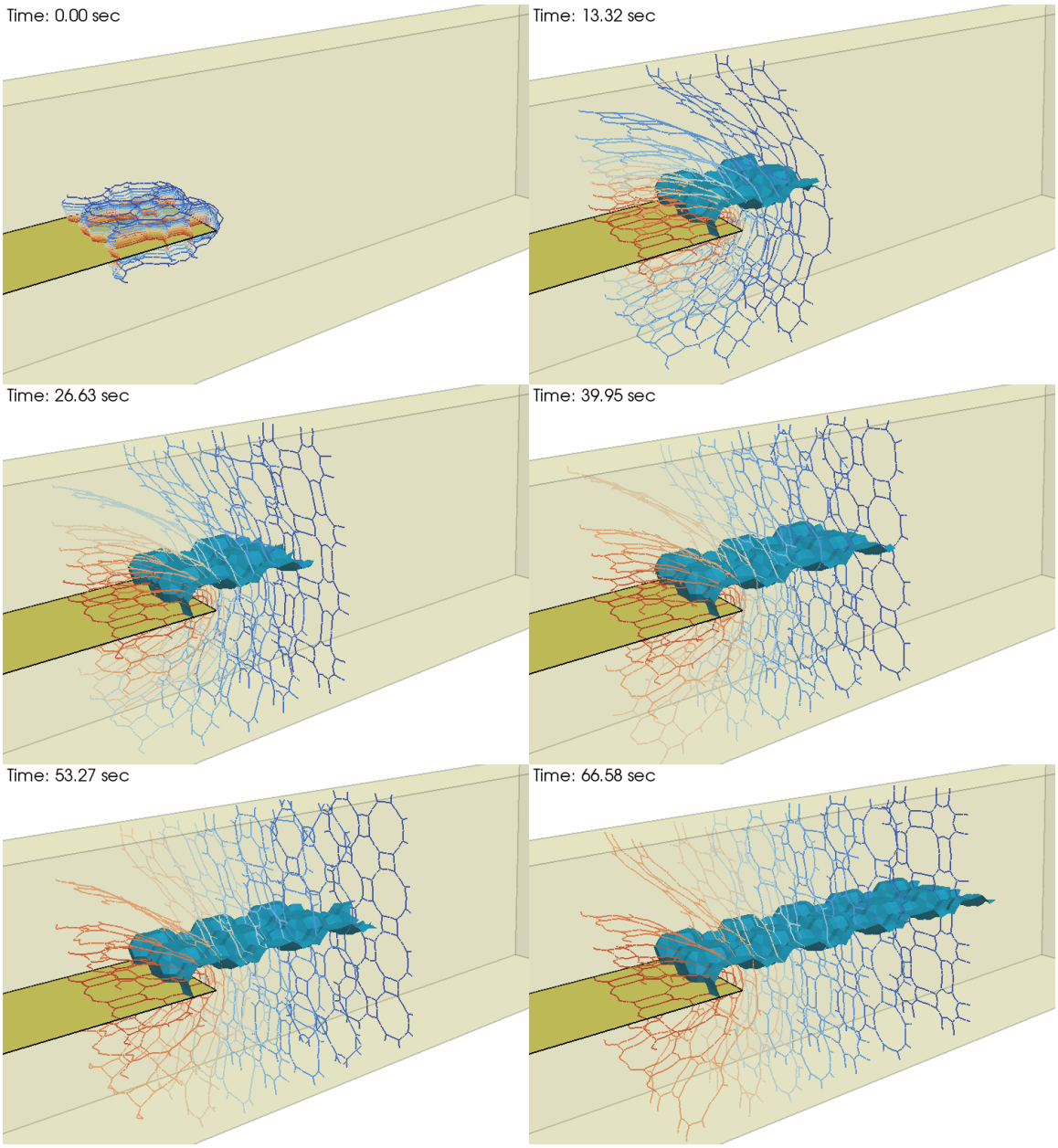

Figure 5.8: Temporal evolution of crack surface. Colored contour levels represent the hydrogen coverage whereas the fracture surface is shown in light blue.

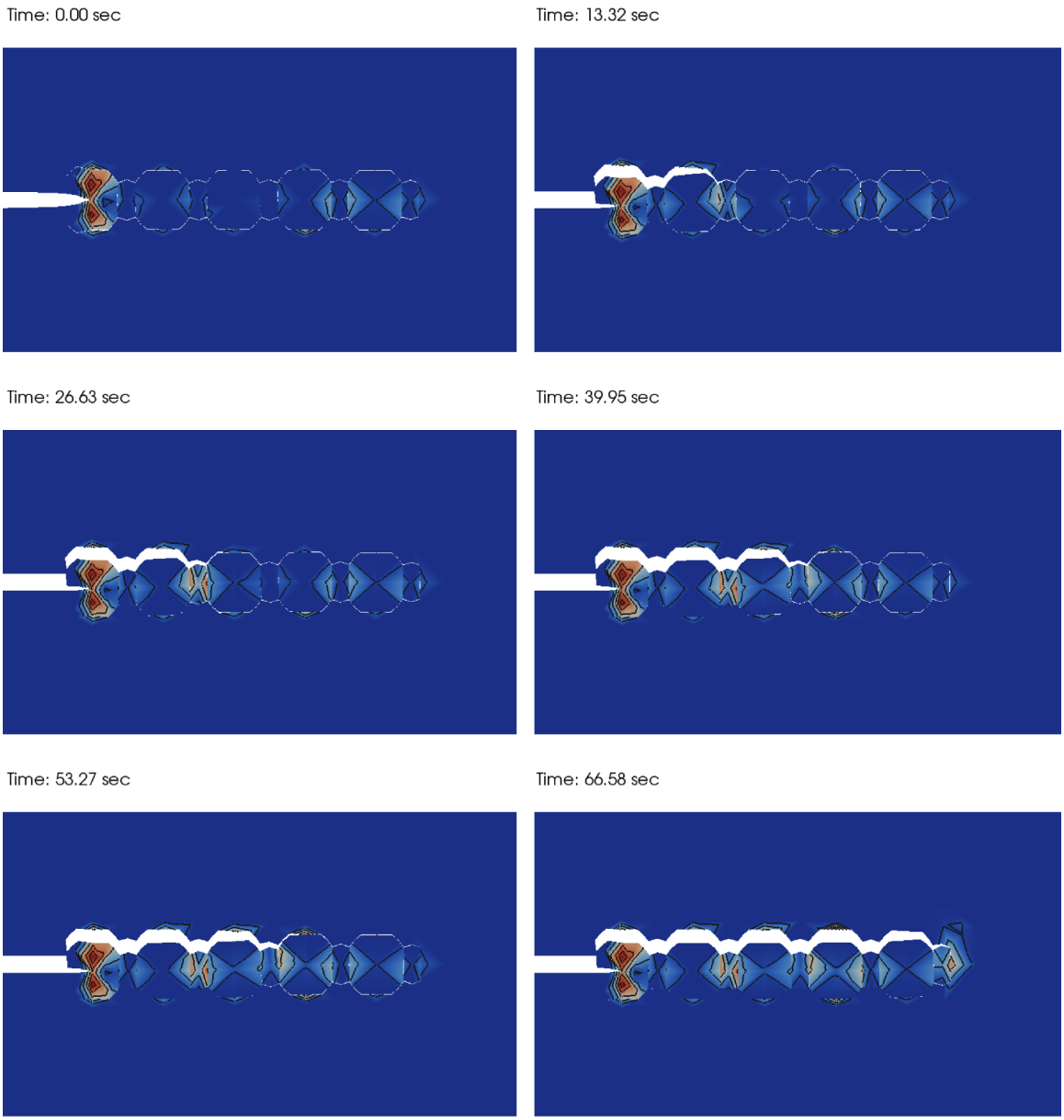

Figure 5.9: Temporal evolution of crack. Color codes denote effective plastic strain.

there was no evident initiation point. Therefore, it was assumed to be the time for which the estimated crack length reaches 200 μm in consistency with all other cases. For levels below this last one crack propagation was not observed after 1,000,000 seconds.

Figure 5.10 shows the computed initiation times vs. the applied stress intensity factor. This plot also depicts the experimental values reported in [6] for validation purposes. As it can be observed, the model predicts the right behavior and the computed values have a good agreement with the reported results. The match is not perfect but a direct comparison cannot be done since the experiments were performed with notched specimens and our model has a singular crack tip. The ability of the model to predict initiation times within a reasonable range is remarkable.

Similar simulations were performed for $D_{gb} = 1.00 \cdot 10^{-9} m^2/sec$ to explore the effect of the grain boundary diffusion coefficient on the model. The results are summarized in figures 5.11 and 5.12.

From figure 5.11 it is possible to conclude that a decrease in the diffusion coefficient results in an increase of the initiation times as expected. Nevertheless, a trend could not be inferred from figure 5.12.

5.3.3 Crack-growth-rate results

As mentioned before, the crack-growth rate was obtained as the slope of the linear fit for the computed crack length time history. Figure 5.13 shows the computed crack-growth-rate as a function of the applied stress intensity factor. Computations for loading levels above 41.2 $MPa\ \sqrt{m}$ were not possible to perform since the initiation jump length exceeded the size of the zone where cohesive elements were placed rendering the results invalid.

The experimental values reported in [7] are also depicted in figure 5.13 for validation

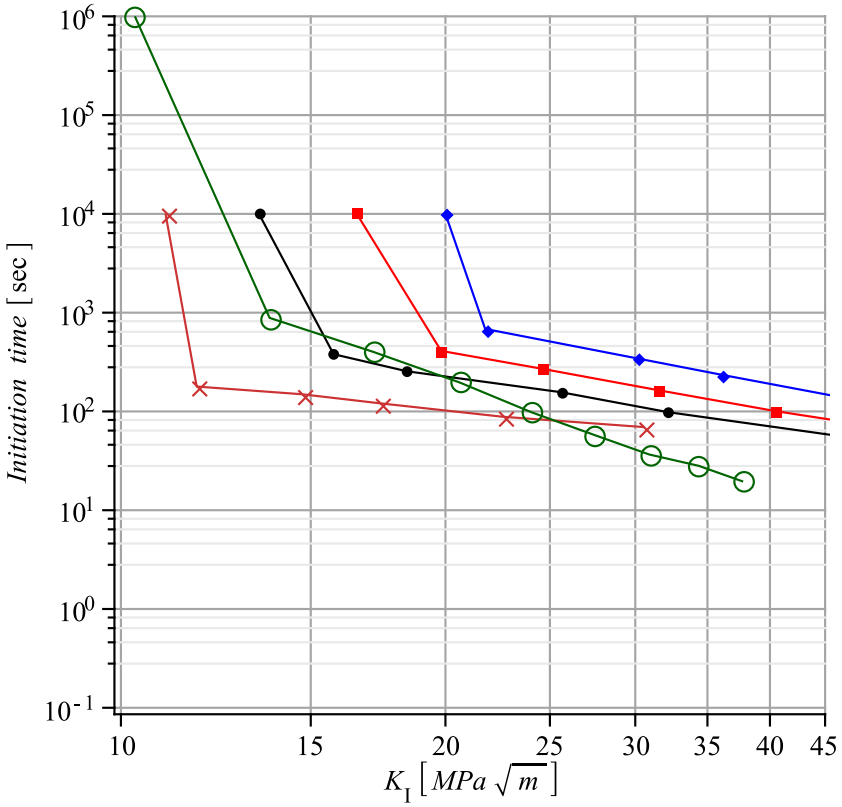

Figure 5.10: Initiation time validation for hydrogen embrittlement of AISI 4340 steel. The computed values (green circles) show a good agreement with the experimental findings of Hirose and Mura [6]. The experimental curves correspond to notch radius 2.5 mm (blue diamonds), 1.0 mm (red squares), 0.5 mm (black solid circles) and 0.25 mm (corsses).

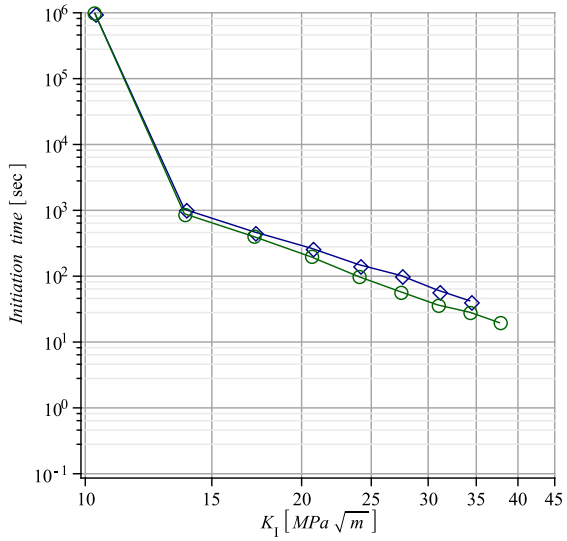

Figure 5.11: Effect of grain boundary diffusion coefficient on initiation time. Green circles correspond to $D_{gb} = 2.53 \cdot 10^{-9} m^2/sec$ whereas blue diamonds correspond to $D_{gb} = 1.0 \cdot 10^{-9} m^2/sec$. A decrease in the diffusion coefficient results in an increase of the initiation times.

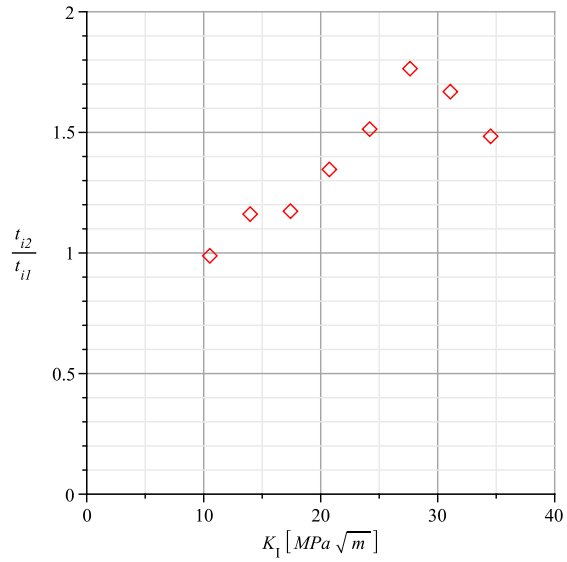

Figure 5.12: Effect of grain boundary diffusion coefficient on initiation time. The ratio $\frac{t_{i1}}{t_{i2}}$ is plotted for several loading levels where t_{i1} and t_{i2} are the initiation times for $D_{gb} = 1.00 \cdot 10^{-9} m^2/sec$ and $D_{gb} = 2.53 \cdot 10^{-9} m^2/sec$ respectively.

purposes. As it can be observed, the model predicts qualitatively the right behavior reported by experiments including:

1. The presence of a threshold intensity factor K_{Iscc} below which there is no crack propagation.

2. The existence of a plateau region for which the crack-growth-rate variation as a function of the applied stress intensity factor is not significant.

3. The occurrence of crack arrest when the stress intensity factor reaches a critical value K_{Ic}.

In addition to capturing the right qualitative behavior, the model was able to make excellent quantitative predictions as well. Computed values have an extraordinary agreement with the results reported in the literature. Thus, we conclude that the model shows excellent potential to predict crack-growth-rates for hydrogen embrittlement and probably for other types of impurity-enhanced decohesion.

To conclude this analysis, similar simulations were performed for $D_{gb} = 1.00 \cdot 10^{-9} m^2/sec$ to explore the effect of the grain boundary diffusion coefficient on the model. The results are summarized in figures 5.14 and 5.15.

From figure 5.15 it is possible to conclude that a decrease in the diffusion coefficient results in a decrease of the crack growth rate as expected. Nevertheless, a trend could not be inferred from figure 5.15.

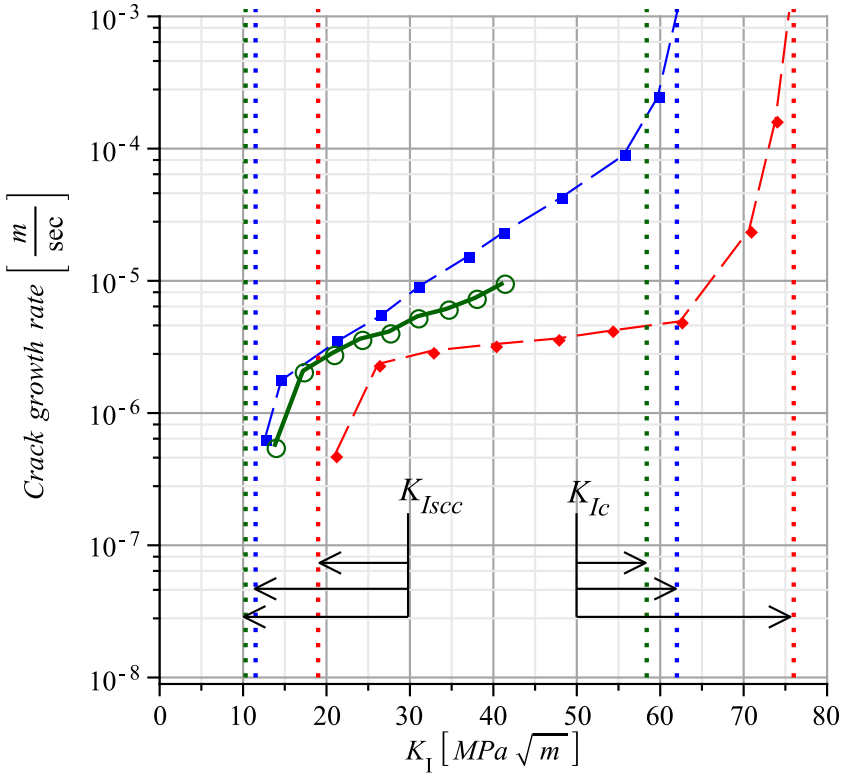

Figure 5.13: Crack growth rate validation for hydrogen embrittlement of AISI 4340 steel. The computed values (green circles) are in excellent agreement with the experimental findings of Hirose and Mura [7].

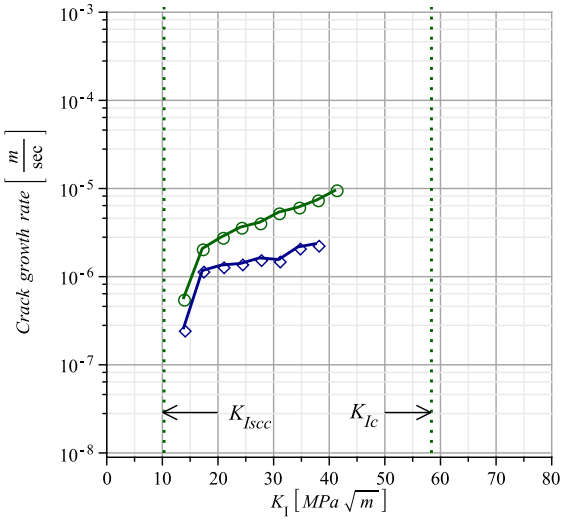

Figure 5.14: Effect of diffusion coefficient on crack growth rate. Green circles correspond to $D_{gb} = 2.53 \cdot 10^{-9} m^2/sec$ whereas blue diamonds correspond to $D_{gb} = 2.53 \cdot 10^{-9} m^2/sec$. A decrease in the diffusion coefficient is accompanied by an increment on the initiation times.

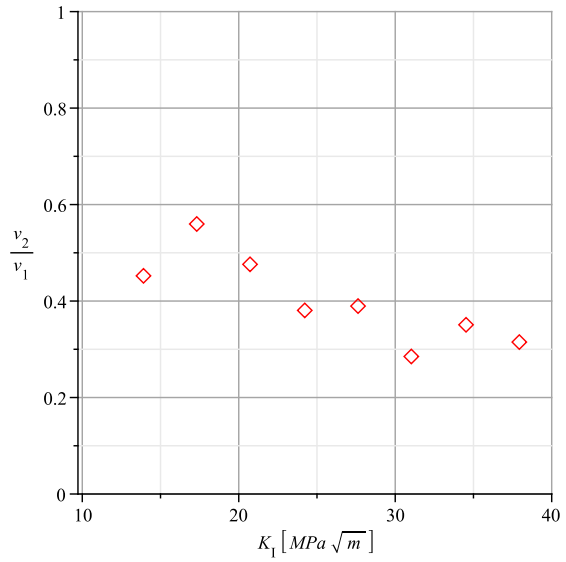

Figure 5.15: Effect of diffusion coefficient on crack growth rate. Green circles correspond to $D_{gb} = 2.53 \cdot 10^{-9} m^2/sec$ whereas blue diamonds correspond to $D_{gb} = 2.53 \cdot 10^{-9} m^2/sec$. A decrease in the diffusion coefficient is accompanied by an increment on the initiation times.

Chapter 6

Conclusions, current work and future directions

6.1 Summary and conclusions

In the present work, a novel 3-dimensional multiphysics model for understanding the intergranular SCC of polycrystalline materials under the effect of impurity-enhanced decohesion was developed. This new model is based upon: (i) a robust algorithm capable of generating the geometry of polycrystals for objects of arbitrary shape; (ii) a continuum finite element model of the crystals including crystal plasticity; (iii) a grain boundary diffusion model informed with first-principles computations of diffusion coefficients; and (iv) an intergranular cohesive model described by concentration-dependent constitutive relations derived from first-principles.

The method developed for generating polycrystalline geometries consists of two main stages: a purely geometric stage where a barycentric dual mesh is generated and the grain domains are defined, and a relaxation stage where the grain boundaries are relaxed to obtain more convex grains.

Besides being very robust, the proposed method showed to be practical for generating polycrystalline structures for complex geometries using as a unique input the mesh repre-

senting the geometry of the object being modeled. The only requirement on the input mesh is that it has to be a simplicial complex of any dimension. In addition, the method showed to be very flexible allowing for the generation of polycrystals with arbitrary distribution of grain sizes.

The predictive capabilities of the intergranular stress corrosion model were assessed by performing simulations of hydrogen embrittlement of AISI 4340 steel in aqueous solution and comparing the obtained results against experimental data available for initiation time and crack-growth-rate tests.

As shown, the model predicts the right behavior for crack nucleation tests. The computed values showed a good agreement with the reported results. The match was not perfect but a direct comparison could not be done since the experiments were performed with notched specimens and our model had a singular crack tip. The ability of the model to predict initiation times within a reasonable range is remarkable.

The model also qualitatively predicts the right behavior reported by crack-growth-rate experiments including:

1. The presence of a threshold intensity factor K_{Iscc} below which there is no crack propagation.

2. The existence of a plateau region for which the crack-growth-rate variation as a function of the applied stress intensity factor is not significant.

3. The occurrence of crack arrest when the stress intensity factor reaches a critical value K_{Ic}.

In addition to capturing the right qualitative behavior, the model was able to make excellent quantitative predictions as well. Computed values had an extraordinary agreement

with the results reported in the literature showing the ability of the model to predict crack-growth-rates for hydrogen embrittlement and probably for other types of impurity-enhanced decohesion.

6.2 Current work and future directions

A logical extension of the work presented in this thesis is the analysis of the effect of grain size on the stress intensity threshold K_{Iscc} and on the crack-growth-rate.

Lessar and Gerberich [97] studied experimentally the grain size effect in hydrogen-assisted cracking. They performed measurements on AISI 4340 steel samples with average grain sizes of 20, 50, 90 and 140 μm. Their investigation shows that increased grain size improved stress corrosion resistance for those cases where the grain diameter was significantly larger than the plastic zone. This increase in the stress corrosion resistance was evidenced by a slight increase in threshold stress intensity K_{Iscc} and an inverse grain-size squared dependence of crack-growth-rate.

As the time of this thesis being submitted, one simulation of hydrogen embrittlement of AISI 4340 steel with the same properties adopted in chapter 5 but average grain size of 50 μm was performed to assess the feasibility of such a study. This simulation took 2 months to conclude and represents just one point for both the initiation time and and crack-growth-rate tests. In order to be able to extract conclusions from this kind of study, at least 6 points would be necessary for 50 μm grain size and another 6 points for 25 μm. With adequate computational resources, we estimate that these simulations could be performed within half a year.

Another interesting direction of future work would be to explore the effects of different models of grain boundary energy on the relaxation stage of the geometry generation

method. The area minimization performed in chapter 2 could be thought of as a grain boundary energy optimization where the energy is kept constant (and independent of grains misorientation and grain boundary orientation) throughout the sample.

Given a physics-based grain boundary energy, it could be added to the polycrystal generation algorithm with a minimum effort. We have been working on this direction lately, more precisely in the formulation of a 5-parameter grain boundary energy.

Bibliography

[1] J.R. Munkres. *Elements of algebraic topology.* Addison Wesley Publishing Company, 1993.

[2] M. Desbrun, E. Kanso, and Y. Tong. Discrete differential forms for computational modeling. In *International Conference on Computer Graphics and Interactive Techniques*, pages 39–54. ACM New York, NY, USA, 2006.

[3] I. Kaur, W. Gust, and L. Kozma. *Handbook of Grain and Interface Boundary Diffusion Data.* Ziegler Press, 1998.

[4] *Military Handbook 5H: Metallic Materials and Elements for Aerospace Vehicle Structures.* US Department of Defense, 1998.

[5] D.E. Jiang and E.A. Carter. First principles assessment of ideal fracture energies of materials with mobile impurities: implications for hydrogen embrittlement of metals. *Acta Materialia*, 52(16):4801–4807, 2004.

[6] Y. Hirose and T. Mura. Nucleation mechanism of stress sorrosion sracking from notches. *Engineering Fracture Mechanics*, 19(2):317–329, 1984.

[7] Y. Hirose and T. Mura. Growth mechanism of stress corrosion cracking in high-strength steel. *Engineering Fracture Mechanics*, 19(6):1057–1067, 1984.

[8] A. Van Duin. Private communication, 2008.

[9] R.H. Jones. *Stress-corrosion Cracking.* ASM International, 1992.

[10] I.A. Johnston. *Understanding and predicting gun barrel erosion.* Australian Government, Department of Defense, 2005.

[11] A.G. Lichtenstein. The Silver Bridge Collapse Recounted. *Journal of Performance of Constructed Facilities*, 7(4):249–261, 1993.

[12] M. Yamaguchi, M. Shiga, and H. Kaburaki. Grain Boundary Decohesion by Impurity Segregation in a Nickel-Sulfur System, 2005.

[13] J.K. Heuer, P.R. Okamoto, N.Q. Lam, and J.F. Stubbins. Disorder-induced melting in nickel: implication to intergranular sulfur embrittlement. *Journal of Nuclear Materials*, 301(2-3):129–141, 2002.

[14] M. Yamaguchi, Y. Nishiyama, and H. Kaburaki. Decohesion of iron grain boundaries by sulfur or phosphorous segregation: First-principles calculations. *Physical Review B*, 76(3):35418, 2007.

[15] U. Krupp, W. Kane, Pfaendtner J.A., X. Liu, C. Laird, and C.J. McMahon Jr. Oxygen-induced intergranular fracture of the nickel-base alloy IN718 during mechanical loading at high temperatures. *Materials Research*, 7, 2004.

[16] K.M. Chang, M.F. Henry, and M.G. Benz. Metallurgical Control of Fatigue Crack Propagation in Superalloys. *JOM*, 42(12):29–35, 1990.

[17] H. Ghonem and D. Zheng. Depth of intergranular oxygen diffusion during environment-dependent fatigue crack growth in alloy 718. *Materials science & engineering. A, Structural materials: properties, microstructure and processing*, 150(2):151–160, 1992.

[18] H. Ghonem, T. Nicholas, and A. Pineau. Elevated temperature fatigue crack growth in alloy 718-Part I: effect of mechanical varibles. *Fatigue & Fracture of Engineering Materials & Structures*, 16(5):565–576, 1993.

[19] H. Ghonem, T. Nicholas, and A. Pineau. Elevated temperature fatigue crack growth in alloy 718-Part II: effects of invironmental and material variables. *Fatigue & Fracture of Engineering Materials & Structures*, 16(6):577–590, 1993.

[20] R. Molins, G. Hochstetter, J.C. Chassaigne, and E. Andrieu. Oxidation effects on the fatigue crack growth behaviour of alloy 718 at high temperature. *Acta Materialia*, 45(2):663–674, 1997.

[21] M. Yamaguchi and H. Kaburaki. First-principles calculations on the grain boundary decohesion of iron and nickel by oxigen. In *Joint International Topical Meeting on Mathematics & Computation and Supercomputing in Nuclear Engineering*. American Nuclear Society, April 2007.

[22] S. Serebrinsky, E.A. Carter, and M. Ortiz. A quantum-mechanically informed continuum model of hydrogen embrittlement. *Journal of the Mechanics and Physics of Solids*, 52(10):2403–2430, 2004.

[23] S. Sopok, C. Rickard, and S. Dunn. Thermal–chemical–mechanical gun bore erosion of an advanced artillery system part one: theories and mechanisms. *Wear*, 258(1-4):659–670, 2005.

[24] S. Sopok, C. Rickard, and S. Dunn. Thermal–chemical–mechanical gun bore erosion of an advanced artillery system part two: modeling and predictions. *Wear*, 258(1-4):671–683, 2005.

[25] C. Bjerken, J.J. Rimoli, and M. Ortiz. Stress corrosion crack growth beneath a stiff coating - influence of chemical potential and interface toughness. *International Conference on Fracture, Ottawa, Canada*, 2009.

[26] M.C. Rivara and C. Levin. A 3-d refinement algorithm suitable for adaptive and multigrid techniques. *Communications in Applied Numerical Methods*, 8:281–290, 1992.

[27] A. Hatcher. *Algebraic Topology*. Cambridge University Press, 2002.

[28] J.C. Fisher. Calculation of Diffusion Penetration Curves for Surface and Grain Boundary Diffusion. *Journal of Applied Physics*, 22:74–77, 1951.

[29] L.G. Harrison. Influence of dislocations on diffusion kinetics in solids with particular reference to the alkali halides. *Transactions of the Faraday Society*, 57:1191–1199, 1961.

[30] M. Ortiz and A. Pandolfi. Finite-deformation irreversible cohesive elements for three-dimensional crack-propagation analysis. *International Journal for Numerical Methods in Engineering*, 44(9):1267–1282, 1999.

[31] C.E. Krill III and L.Q. Chen. Computer simulation of 3-D grain growth using a phase-field model. *Acta Materialia*, 50:3057–3073, 2002.

[32] G. Russo and P. Smereka. A level-set method for the evolution of faceted crystals. *SIAM Journal on Scientific Computing*, 21(6):2073–2095, 2000.

[33] Z. Zhao, S. Kuchnicki, R. Radovitzky, and A. Cuitino. Influence of in-grain mesh resolution on the prediction of deformation textures in fcc polycrystals by crystal plasticity FEM. *Acta Materialia*, 55(7):2361–2373, 2007.

[34] A. Jérusalem, M. Dao, S. Suresh, and R. Radovitzky. Three-dimensional model of strength and ductility of polycrystalline copper containing nanoscale twins. *Acta Materialia*, 56(17):4647–4657, 2008.

[35] S. Elcott and P. Schröder. Building your own dec at home. In *International Conference on Computer Graphics and Interactive Techniques*. ACM New York, NY, USA, 2005.

[36] M. Ortiz. *Computational Mechanics Course Notes*. California Institute of Technology, 2008.

[37] I. Kaur, Y. Mishin, and W. Gust. *Fundamentals of Grain and Interface Boundary Diffusion*. John Wiley and Sons LTD, 1995.

[38] A. Fick. Ueber Diffusion. *Annalen der Physik*, 170(1):59–86, 1855.

[39] Y.M. Mishin and I.V. Yurovitskii. A generalized model of grain boundary diffusion. *Philosophical Magazine A*, 64(6):1239–1249, 1991.

[40] L. Klinger and E. Rabkin. Diffusion along the Grain Boundaries in Crystals with Dislocations. *Interface Science*, 6(3):197–203, 1998.

[41] L. Klinger and E. Rabkin. Beyond the Fisher model of grain boundary diffusion: effect of structural inhomogeneity in the bulk. *Acta Materialia*, 47(3):725–734, 1999.

[42] Y. Mishin and C. Herzig. Grain boundary diffusion: recent progress and future research. *Materials Science and Engineering: A*, 260(1):55–71, 1999.

[43] A. Atkinson. Grain-boundary diffusion: an historical perspective. *Journal of the Chemical Society, Faraday Transactions*, 86(8):1307–1310, 1990.

[44] F. Güthoff, Y. Mishin, and C. Herzig. Self-diffusion along stationary and moving grain boundaries in α-Hf. *Zeitschrift für Metallkunde*, 84(8):584–591, 1993.

[45] E.W. Hart. On the role of dislocations in bulk diffusion. *Acta Metallurgica*, 5:597, 1957.

[46] J.E. Marsden and T.J.R. Hughes. *Mathematical Foundations of Elasticity*. Dover Publications, 1994.

[47] M.E. Gurtin. *An Introduction to Continuum Mechanics*. Academic Press, 1981.

[48] J. Lubliner. On the thermodynamic foundations of non-linear solid mechanics. *International Journal of Non-Linear Mechanics*, 7(3):237–254, 1972.

[49] J. Lubliner. On the structure of the rate equations of materials with internal variables. *Acta Mechanica*, 17(1):109–119, 1973.

[50] F. Armero. Elastoplastic and Viscoplastic Deformations in Solids and Structures. *Encyclopedia of Computational Mechanics*, 2:227–266, 2004.

[51] F. Armero and J.C. Simo. A new unconditionally stable fractional step method for non-linear coupled thermomechanical problems. *International Journal for Numerical Methods in Engineering*, 4:737–766, 1992.

[52] F. Armero and J.C. Simo. A priori stability estimates and unconditionally stable product formula algorithms for nonlinear coupled thermoplasticity. *International journal of plasticity*, 9(6):749–782, 1993.

[53] G.T. Camacho and M. Ortiz. Computational modelling of impact damage in brittle materials. *International Journal of Solids and Structures*, 33:2899–2938, 1996.

[54] G.T. Camacho and M. Ortiz. Adaptive Lagrangian modelling of ballistic penetration of metallic targets. *Computer Methods in Applied Mechanics and Engineering*, 142(3-4):269–301, 1997.

[55] T.D. Marusich and M. Ortiz. Modelling and simulation of high-speed machining. *International Journal for Numerical Methods in Engineering*, 38(21):3675–3694, 1995.

[56] G.I. Taylor. Plastic strain in metals. *Journal of the Institute of Metals*, 62(1):307–324, 1938.

[57] R. Hill. Generalized constitutive relations for incremental deformation of metal crystals by multislip. *Journal of the Mechanics and Physics of Solids*, 14(4):95–102, 1966.

[58] J.R. Rice. Inelastic constitutive relations for solids: an internal variable theory and its application to metal plasticity. *Journal of the Mechanics and Physics of Solids*, 19(6):433–455, 1971.

[59] J. Kratochvil. Finite-strain theory of crystalline elastic-inelastic materials. *Journal of Applied Physics*, 42(3):1104–1108, 1971.

[60] R. Hill and J.R. Rice. Constitutive analysis of elastic-plastic crystals at arbitrary strain. *Journal of the Mechanics and Physics of Solids*, 20(6):401–413, 1972.

[61] K.S. Havner. On the mechanics of crystalline solids. *Journal of the Mechanics and Physics of Solids*, 21(6):383–394, 1973.

[62] R.J. Asaro and J.R. Rice. Strain localization in ductile single crystals. *Journal of the Mechanics and Physics of Solids*, 25(5):309–338, 1977.

[63] R. Hill and K.S. Havner. Perspectives in the mechanics of elastoplastic crystals. *Journal of the Mechanics and Physics of Solids*, 30(1-2):5–22, 1982.

[64] C. Miehe and J. Schotte. Crystal plasticity and evolution of polycrystalline microstructure. *Encyclopedia of Computational Mechanics*, 2:267–289, 2004.

[65] V.A. Lubarda. *Elastoplasticity Theory.* CRC Press, 2002.

[66] JW Hutchinson. Elastic-Plastic Behaviour of Polycrystalline Metals and Composites. *Proceedings of the Royal Society of London. Series A, Mathematical and Physical Sciences (1934-1990)*, 319(1537):247–272, 1970.

[67] D. Peirce, R.J. Asaro, and A Needleman. Material rate dependence and localized deformation in crystalline solids. *Acta Metallurgica*, 31(12):1951–1976, 1983.

[68] J.L. Bassani and T.Y. Wu. Latent Hardening in Single Crystals II. Analytical Characterization and Predictions. *Proceedings of the Royal Society: Mathematical and Physical Sciences*, 435:21–41, 1991.

[69] A.M. Cuitino and M. Ortiz. Computational modelling of single crystals. *Modelling and Simulation in Materials Science and Engineering*, 1:225–263, 1993.

[70] J.C. Simo and T.J.R. Hughes. *Computational Inelasticity.* Springer, 1998.

[71] M. Ortiz and E.P. Popov. Accuracy and stability of integration algorithms for elastoplastic constitutive relations. *International Journal for Numerical Methods in Engineering*, 21(9), 1985.

[72] M. Ortiz and L. Stainier. The variational formulation of viscoplastic constitutive updates. *Computer Methods in Applied Mechanics and Engineering*, 171(3-4):419–444, 1999.

[73] D.P. Bertsekas. *Nonlinear programming.* Athena Scientific Belmont, Mass, 1999.

[74] D.S. Dugdale. Yielding of steel sheets containing slits. *Journal of the Mechanics and Physics of Solids*, 8(2):100–104, 1960.

[75] G.I. Barenblatt. The Mathematical Theory of Equilibrium Cracks in Brittle Fracture. *Advances in Applied Mechanics*, 7:55–129, 1962.

[76] J.R. Rice. Mathematical analysis in the mechanics of fracture. *Fracture: An Advanced Treatise*, 2:191–311, 1968.

[77] A. Hillerborg, M. Modeer, P.E. Petersson, et al. Analysis of crack formation and crack growth in concrete by means of fracture mechanics and finite elements. *Cement and Concrete Research*, 6(6):773–782, 1976.

[78] A. Carpinteri. *Mechanical Damage and Crack Growth in Concrete: Plastic Collapse to Brittle Fracture*. Springer, 1986.

[79] A. Needleman. A continuum model for void nucleation by inclusion debonding. *Journal of Applied Mechanics*, 54(3):525–531, 1987.

[80] A. Needleman. An analysis of decohesion along an imperfect interface. *International Journal of Fracture*, 42(1):21–40, 1990.

[81] A. Needleman. Micromechanical modelling of interfacial decohesion. *Ultramicroscopy*, 40(3):203–214, 1992.

[82] G. Xu and M. Ortiz. A Variational Boundary Integral Method for the Analysis of 3-D Cracks of Arbitrary Geometry Modelled as Continuous Distributions of Dislocation Loops. *International Journal for Numerical Methods in Engineering*, 36:3675–3675, 1993.

[83] V. Tvergaard and J.W. Hutchinson. The influence of plasticity on mixed mode interface toughness. *Journal of the Mechanics and Physics of Solids*, 41(6):1119–1135, 1993.

[84] J. Planas, M. Elices, and G.V. Guinea. Book chapter: cohesive cracks as a solution of a class of nonlocal problems. *Fracture and Damage in Quasibrittle Structures. Experiment, Modelling and Computer Analysis, Bazant ZP (ed.). E & FN SPON*, 1994.

[85] V. Tvergaard and J.W. Hutchinson. Effect of strain dependent cohesive zone model on predictions of interface crack growth. *Journal de Physique IV*, 6(C6):165–172, 1996.

[86] V. Tvergaard and J.W. Hutchinson. Effect of strain-dependent cohesive zone model on predictions of crack growth resistance. *International Journal of Solids and Structures*, 33(20-22):3297–3308, 1996.

[87] K. Willam, T. Stankowski, K. Runesson, and S. Sture. Simulation issues of distributed and localized failure computations. *Cracking and Damage, Mazars J, Bazant ZP (eds). Elsevier Science: New York*, pages 363–378, 1989.

[88] M. Ortiz and S. Suresh. Statistical properties of residual stresses and intergranular fracture in ceramic materials. *Journal of Applied Mechanics*, 60(1):77–84, 1993.

[89] X.P. Xu and A. Needleman. Numerical simulations of fast crack growth in brittle solids. *Journal of the Mechanics and Physics of Solids*, 42:1397–1397, 1994.

[90] X.P. Xu and A. Needleman. Numerical simulations of dynamic crack growth along an interface. *International Journal of Fracture*, 74:289–324, 1995.

[91] A. Van der Ven and G. Ceder. Impurity-induced van der Waals transition during decohesion. *Physical Review B*, 67(6):60101, 2003.

[92] G.H. Lu, Y. Zhang, S. Deng, T. Wang, M. Kohyama, R. Yamamoto, F. Liu, K. Horikawa, and M. Kanno. Origin of intergranular embrittlement of Al alloys induced by Na and Ca segregation: Grain boundary weakening. *Physical Review B*, 73(22):224115, 2006.

[93] Y. Zhang, G. Lu, T. Wang, S. Deng, X. Shu, M. Kohyama, and R. Yamamoto. First-principles study of the effects of segregated Ga on an Al grain boundary. *Journal of Physics: Condensed Matter*, 18(22):5121–5128, 2006.

[94] Y. Zhang, G.H. Lu, S. Deng, T. Wang, H. Xu, M. Kohyama, and R. Yamamoto. Weakening of an aluminum grain boundary induced by sulfur segregation: A first-principles computational tensile test. *Physical Review B*, 75(17):174101, 2007.

[95] C.A. Felippa, KC Park, and C. Farhat. Partitioned analysis of coupled mechanical systems. *Computer Methods in Applied Mechanics and Engineering*, 190(24-25):3247–3270, 2001.

[96] C.D. Beachem. A new model for hydrogen-assisted cracking (hydrogen embrittlement). *Metallurgical and Materials Transactions B*, 3(2):441–455, 1972.

[97] J.F. Lessar and W.W. Gerberich. Grain size effects in hydrogen-assisted cracking. *Metallurgical and Materials Transactions A*, 7(6):953–960, 1976.

[98] W.T. Read and W. Shockley. Dislocation models of crystal grain boundaries. *Physical Review*, 78(3):275–289, 1950.